Modeling of unrest signals in heterogeneous hydrothermal systems

M. Todesco[1], A. P. Rinaldi[1,2], M. Bonafede[2]

M. Bonafede, Dipartimento di Fisica, Settore Geofisica, Università di Bologna, viale Berti Pichat, 8, 40127 Bologna, Italy. (maurizio.bonafede@unibo.it)

A. P. Rinaldi, M. Todesco, Istituto Nazionale di Geofisica e Vulcanologia, via Donato Creti, 12, 40128 Bologna, Italy. (rinaldi@bo.ingv.it, todesco@bo.ingv.it)

[1]Istituto Nazionale di Geofisica e Vulcanologia, Sezione di Bologna, Italy.

[2]Dipartimento di Fisica, Settore Geofisica, Università di Bologna, Italy.

Abstract. Monitoring of quiescent volcanoes, such as Campi Flegrei (Italy), involves the measurement of geochemical and geophysical parameters that are expected to change as eruptive conditions approach. Some of these changes are associated with the hydrothermal activity that is driven by the release of heat and magmatic fluids. This work focuses on the properties of the porous medium and on their effects on the signals generated by the circulating fluids. The TOUGH2 porous media flow model is applied to simulate a shallow hydrothermal system fed by a source of magmatic fluids. The simulated activity of the source, with periods of increased fluid discharge, generates changes in gas composition, gravity, and ground deformation. The same boundary conditions and source activity were applied to simulate the evolution of homogeneous and heterogeneous systems, characterized by different rock properties. Phase distribution, fluid composition, and the related signals depend on the nature and properties of the rock sequence through which the fluids propagate. Results show that the distribution of porosity and permeability affects all the observable parameters, controlling the timing and the amplitude of their changes through space and time. Preferential pathways for fluid ascent favor a faster evolution, with larger changes near permeable channels. Slower changes over wider areas characterize less permeable systems. These results imply that monitoring signals do not simply reflect the evolution of the magmatic system: intervening rocks leave a marked signature that should be taken into account when monitoring data are used to infer system conditions at depth.

1. Introduction

The evolution of hydrothermal activity is monitored in many active volcanic areas, such as Campi Flegrei (Italy), because of its relation to the magmatic system at depth. A magmatic component is commonly recognized in the fluids discharged in volcanic areas: the abundance, temperature, and composition of this component are expected to change as the volcano approaches eruptive conditions. Significant changes in the magmatic system that feeds the hydrothermal circulation should be accompanied by measurable changes of observable parameters such as gas composition, temperature, flow rate, or the extent of the degassing area. Several geophysical parameters also depend on circulating hydrothermal fluids and hence reflect changes in the magmatic source: gravity is affected by the underground redistribution of gas and liquid phases, and by their composition; changes in pore pressure and fluid temperature act on the porous rock and may cause significant amounts of ground deformation [*Todesco et al.*, 2004; *Hurwitz et al.*, 2007; *Hutnak et al.*, 2009; *Rinaldi et al.*, 2010].

Monitoring carried out at the Campi Flegrei caldera during the last 40 years highlighted different unrest phases, when all of the mentioned observables underwent changes, followed by quiet periods. Two major episodes of unrest occurred in 1969-72 and 1982-84 and were accompanied by remarkable ground displacement (or bradyseism): the maximum uplift was measured at the caldera center, near the town of Pozzuoli, and reached values up to +1.7 m, in 1972, and +1.8 m, in 1984. A long lasting subsidence begun in 1985, and was periodically interrupted by minor (cm), short-lasting (months) uplifts in 1989, 1994, 2000, and 2006. Each unrest episode, either large or small, was accompanied by

changes of various geochemical and geophysical parameters. Shallow seismicity (< 4 km) was recorded during each uplift phases, and in 1984 caused the evacuation of the town of Pozzuoli. Gravity changes are also measured within the caldera, with greater changes observed near the caldera center [*Barberi et al.*, 1984; *Berrino et al.*, 1984; *Orsi et al.*, 1999; *Troise et al.*, 2007]. The caldera hosts a large hydrothermal system which feeds fumarolic activity and diffuse degassing both offshore and inland [*Allard et al.*, 1991; *De Natale et al.*, 1991; *Tedesco et al.*, 1990; *Tedesco*, 1994]. Inland, the hydrothermal activity is mostly concentrated within the Solfatara crater, close to the caldera center. During each unrest event, the composition of fumarolic gases changed through time, with an increase of the relative content of magmatic CO_2. Maximum CO_2 enrichment are reached several months after the maximum uplift. Changes were detected also in the rate of diffuse ground degassing and in the size of the degassing area [*Chiodini et al.*, 2001, 2003, 2009; *Chiodini*, 2009]. The unrest events at Campi Flegrei, as at other calderas, have been interpreted in the literature as driven by magmatic processes at depth, involving the ascent of heat and magmatic fluids [*Newhall and Dzurisin*, 1988; *Sorey et al.*, 2003; *Villemant et al.*, 2005]. Interactions between deep magmatic gases and the shallower hydrothermal system can be regarded as the potential trigger for most of the phenomena observed during recent unrest periods at Campi Flegrei [*Battaglia et al.*, 2006; *Bodnar et al.*, 2007; *Casertano et al.*, 1976; *Chiodini et al.*, 2001, 2003; *Chiodini*, 2009; *De Natale et al.*, 2001; *Lima et al.*, 2009; *Orsi et al.*, 1996, 1999]. Numerical modeling of hydrothermal fluid circulation has shown that the observed trends depend on the temporal evolution of a deep source of magmatic fluids [*Chiodini et al.*, 2003; *Todesco and Berrino*, 2005]. Fumarole composition and especially gravity were shown to be sensitive to the properties and evolution of the

deep source of fluids, and in particular, to the rate at which magmatic fluids enter the hydrothermal circulation [*Todesco*, 2009]. A significant fraction of the ground deformation observed during the unrest episodes can also be ascribed to changes in the circulation of hydrothermal fluids and the associated thermal and mechanical effects [*Todesco et al.*, 2004; *Rinaldi et al.*, 2010].

The existence of a relation between the evolution of a magmatic source at depth and different observable parameters is the conceptual base for interpretation of monitoring data and for short-term hazard evaluation. However, different processes, possibly unrelated to the presence of a degassing magma body, may lead to similar changes, so that the interpretation of monitoring data is not always straightforward [*Todesco*, 2008, 2009]. The properties of the host rocks influence the way in which different signals are generated and transmitted to the surface. This is particularly relevant at Campi Flegrei where seismic data have shown the presence of large heterogeneities at shallow depths, likely to be associated with the presence of fluids [*Judenherc and Zollo*, 2004; *Chiarabba and Moretti*, 2006; *Tramelli et al.*, 2006; *Bruno et al.*, 2007; *Zollo et al.*, 2008]. Large contrasts between the elastic properties of different rock layers are known to affect the pattern of deformation [*Crescentini and Amoruso*, 2007; *Amoruso et al.*, 2007] while differences in porosity and permeability are expected to control the propagation of the circulating fluids and the distribution of the fluid phases.

In this work, we focus on the effects of rock properties and their spatial distribution on the evolution of selected observables. Numerical simulations run with the same boundary conditions highlight differences that arise from the assumption of different permeabilities, for both homogeneous and heterogeneous systems. Results show that the characteristics

of the porous medium substantially control the response of the hydrothermal system to the applied boundary conditions, controlling both the range of variation and the temporal evolution of the observable signals. These results emphasize the importance of a careful definition of in situ rock properties and suggest a great caution when monitored signals are used to infer magmatic conditions.

2. The simulated hydrothermal system

This paper follows previous research works aimed at interpretation of monitoring data collected at the Campi Flegrei caldera [*Todesco et al.*, 2003; *Chiodini et al.*, 2003; *Todesco et al.*, 2004; *Todesco and Berrino*, 2005; *Todesco*, 2009; *Rinaldi et al.*, 2010]. According to the conceptual model developed for this caldera, its recent evolution has been controlled by a pulsating source of magmatic fluids, with unrest periods characterized by higher flow rate and CO_2 content [*Chiodini et al.*, 2003]. Numerical simulations of hydrothermal fluid circulation were performed with the TOUGH2 model [*Pruess et al.*, 1999] and describe the coupled flow of heat and fluids within a shallow hydrothermal system fed by a deeper source of hot water vapor and CO_2. Modeling results were compared with observed gas composition and gravity data in order to define the source behavior, i.e., assign the timing, flow rates and gas composition for both the unrest and the quiet periods [*Chiodini et al.*, 2003; *Todesco and Berrino*, 2005]. Following this procedure, and applying the same model, we simulate here the same sequence of unrest and quiet periods (Table 1). In this case, we investigate how heterogeneous rock properties affect the evolution of selected observables parameters, compared to results obtained employing a homogeneous domain.

The two-dimensional, axisymmetric computational domain is 10 km wide radially and 1.5 km deep: it was discretized into 2580 elements with radial dimensions ranging from 25

to 3196 m and thickness from 5 to 25 m. The inlet of hot fluids is placed at the bottom of the domain, near the symmetry axis, and injects fluids at fixed enthalpy (corresponding to ca. 623 K). The composition of injected fluids is reported in Table 1 for both the unrest and the quiet times.

Relative permeability is described according to the function proposed by *Corey* [1954], with irreducible gas and liquid saturations of 0.05 and 0.33, respectively. Capillary pressure is calculated as a linear function of liquid saturation, where saturation is above the irreducible value, and is set equal to 0.01 MPa, for liquid fractions below the irreducible saturation.

The different rock domains that characterize the heterogeneous systems are shown in Figure 1. Three horizontal layers are chosen to represent the shallow stratigraphy of the Campi Flegrei caldera, where a rather continuous layer of Neapolitan Yellow Tuff separates more permeable shallow rocks from the deeper and older volcanics and marine sediments emplaced after the Campanian Ignimbrite eruption [*Orsi et al.*, 1996; *Rosi and Sbrana*, 1987]. A high-permeability channel is placed at the symmetry axis to represent the feeding system for the fumaroles at Solfatara, the major site of gas discharge in the caldera. The effective heat and fluid transfer underneath Solfatara is likely due to the presence of highly fractured and permeable materials. The permeable channel is as wide as the Solfatara crater. In some simulation, a transition zone with intermediate values of rock permeability is placed between the vertical channel and the horizontal layers.

The choice of the permeability to assign to the different rock domain in the model is a delicate task. Permeability can vary over orders of magnitude: changes with rock type, with depth and degree of alteration, and evolves through time [*Ingebritsen and Manning*,

2010; *Manning and Ingebritsen*, 1999]. Some permeability measurements were carried out on rock samples at Campi Flegrei. According to these data, permeability of the Neapolitan Yellow Tuff ranges from 10^{-14} to 10^{-13} m^2, whereas samples from the Campanian Ignimbrite range from $1.6x10^{-16}$ to 10^{-13} m^2[*Peluso and Arienzo*, 2007; *Vanorio et al.*, 2002]. Some data also derive from the deep geothermal drillings: permeability values were obtained from core samples and well test data but only for the wells in the western portion of the caldera (Mofete area) [*Rosi and Sbrana*, 1987]. These permeability values are scattered over a wide range, regardless to the sampling depth (10^{-17} to 10^{-13}, with most of the value within 10^{-16} and 10^{-14}). Porosity is also characterized by a large variability, ranging from 0.05 to 0.4, with the largest values associated to the shallowest rocks [*Rosi and Sbrana*, 1987]. The choice of rock properties illustrated in Tables 2, 3, and 4 is based on these data, and on modeling results. The four considered permeability distributions do not explore the entire range of possible permeability values, but clearly illustrate the influence of this parameter on the evolution of the hydrothermal circulation.

In each simulation, the initial conditions are obtained by simulating a long-lasting (thousands of years) injection of magmatic fluids, and represent the steady state conditions associated with the specific distribution of rock properties in each considered case. Starting from these initial conditions, the sequence of unrest and quiet periods taken from *Todesco and Berrino* [2005] is simulated for each considered permeability distribution.

3. The observable parameters

The observable parameters calculated from each simulation include fumarole composition, gravity changes, and the ground deformation caused by the circulation of hydrothermal fluids. Gas composition is expressed as the molar ratio CO_2/H_2O, and is evaluated

near the surface, where a single-phase gas region forms. According to geochemical data, the fumaroles at Solfatara equilibrate within such a shallow dry-gas region before discharging at the surface [*Chiodini et al.*, 2003]. Gas composition is computed here by averaging the composition of all the grid blocks that belong to this shallow dry-gas region. Gravity changes may arise during volcanic unrest because of subsurface mass redistribution, as in the case of shallow magmatic intrusion, or because of ground deformation, which may displace layers of different densities or directly affect the density of rocks through dilatation or contraction. If deformation is caused by an isotropic source embedded in a homogeneous medium, the gravity change due to that deformation is zero [*Walsh and Rice*, 1979], but significant effects could arise if heterogeneous rocks are present [*Amoruso et al.*, 2008]. At this time, however, we neglect the gravity changes arising from ground deformation or magma intrusion, and focus on the effects associated with the circulation of hydrothermal fluids. Gravity changes arise as fluid density evolves through time, due mainly to a variable distribution of liquid and gas within the system. Previous results have shown that the signals generated by the hydrothermal system alone can be of the same order of magnitude of the observed gravity residuals (obtained after correction for ground deformation using a measured free-air gradient) [*Todesco and Berrino*, 2005], implying that this contribution should be quantified and cannot be neglected where a wide hydrothermal system is present. Rock permeability affects the distribution of the fluid phases, and therefore may affect the gravity changes recorded at the surface. At any given time, the gravity change with respect to the initial conditions can be calculated by summing the contribution of each element of the computational mesh. At the surface,

and for an observation point placed at the symmetry axis, the vertical component of the gravity acceleration at a given time is [*Todesco and Berrino*, 2005]:

$$\Delta g_z = \sum GV\phi\Delta\rho_f \frac{z}{R^3} \tag{1}$$

where G is the gravitational constant; V is the volume of the pore space within each grid element;ϕ is the rock porosity; $\Delta\rho_f$ is the change of the average fluid density in the element, with respect to its initial value; z is the depth of the grid element; $R^2 = r^2 + z^2$ is the distance of the grid element from the observation point; and r is the radial distance of the grid element from the symmetry axis.

Also in the case of ground displacement, we focus on the effects due to the hydrothermal fluid circulation. As the fluids propagate, heating and pore pressure changes act on the porous matrix and deform it. At this time, we neglect the effects that such deformation may have on the hydraulic properties of the medium: rock permeability and porosity do not change throughout the simulation. This approach, with a one-way coupling between fluid flow and deformation, was used also by *Todesco et al.* [2004]; *Hurwitz et al.* [2007]; *Hutnak et al.* [2009]; *Rinaldi et al.* [2010] to obtain a first order estimate of ground displacement associated with hydrothermal circulation.

Ground displacement is calculated here using a mathematical model based on the linear theory of thermo-poro-elasticity and on a system of distributed equivalent forces [*Rinaldi et al.*, 2010]. Each grid block of the computational domain is considered as a potential source of deformation, and the final displacement is computed as a sum of the contribution of each element of the mesh.

202 At the symmetry axis, the vertical component of ground displacement u_z can be com-
203 puted, at a given time, as:

$$u_z = \sum \frac{(1+\nu)}{3\pi\mu} \Delta\theta V \frac{z}{R^3} \tag{2}$$

204 where ν is the Poisson's ratio; μ is the rigidity; $\Delta\theta$ represents the dilatation (contraction)
205 due to pressure and temperature changes within the grid element, and is defined as $\Delta\theta =$
206 $(\Delta p/H + \alpha_s \Delta T)$ where $1/H = 1/K - 1/K'_s$ is the Biot's constant; K is the isothermal,
207 drained bulk modulus of the rock; K'_s is the bulk modulus for the solid constituent alone,
208 and α_s is the coefficient of volumetric thermal expansion; V and z are the volume and
209 depth of the element; and R is its distance from the observation point.

210 This approach assumes that the elastic properties of the rocks, shown in Table 5, are
211 homogeneous throughout the system. In this work, such assumption implies that hetero-
212 geneous systems are composed by rocks that have different permeabilities but the same
213 elastic properties. We are aware that the one-way coupling between hydraulic and me-
214 chanical processes and the assumption of homogeneous elastic properties represent a very
215 crude approximation of the natural system, which will not provide a realistic description
216 of the expected deformation. Nevertheless, we can use this theoretical exercise to high-
217 light the role of rock permeability on the pattern of deformation caused by the simulated
218 unrest.

219 Radial patterns of changes of gravity and vertical displacement were also calculated at
220 different times, to investigate spatial variation of these observables.

4. Homogeneous permeability values and associated initial conditions

This section investigates how the value of rock permeability affects the evolution towards steady state conditions in a homogeneous system. Three simulations were run, starting from the same initial geothermal gradient (120 K/km) and hydrostatic pressure profile but with different values of isotropic rock permeability, in the range 10^{-13}-10^{-15} m^2. Other rock properties are listed in Table 2. In each case, hot fluids are continuously injected at the base of the system, close to the axis, until the steady state is reached. Flow rate and fluid composition are the same in each simulation and correspond to the quiet-period values reported in Table 1. Different values of rock permeability affect the final conditions that characterize the steady state in each case. The steady-state distribution of volumetric gas fraction and temperature is compared for the three considered cases in Figure 2. In all three cases, fluid injection causes the development of a hot, two-phase plume. When the permeability is high (HO1, κ=10^{-13} m^2), hot fluids can freely propagate upwards and reach the surface within a few years. The two-phase plume that forms is very narrow (ca. 200 m at the base and 400 m near the surface) and, at its top, a small, dry-gas region forms within ca. 30 years, where there is no liquid water. At steady-state, the heated region remains close to the symmetry axis, while vigorous convection ensures an effective recharge of cold water through the top of the domain and keeps most of the system at a rather low average temperature (300 K).

In the other two simulations, fluid movement is hindered by lower permeability values. In these cases, the continuous fluid supply at the base is not quickly compensated by a corresponding discharge at the top of the domain. Both pressure and temperature increase in the source region and a wider two-phase zone develops with time. In the intermediate-

permeability case (HO2, κ=10^{-14} m^2) the plume is 300 m wide at the base and 1000 m near the surface and hosts a larger dry-gas region. In the third case (HO3, κ=10^{-15} m^2), the steady state is characterized by a wide two-phase plume (more than 1 km at the surface) and high CO_2 mass fractions are achieved near the top of the domain. However, the single-phase gas region never forms.

In all three cases, the inflow of hot fluids is accompanied by ground deformation associated with an increment in pore pressure and temperature within the system (Figure 3). Pressure and temperature changes are faster and smaller for the more permeable system, while greater changes take place more gradually in the less permeable case. These changes deform the porous medium through time. Although these simulations evolve through thousands of years, and therefore transcend the time scale of monitoring systems, we can still compute and compare the ground displacement that arises as each system moves away from its initial linear P,T profiles. The computed ground deformation changes significantly for different values of rock permeability. Figure 3a compares the vertical displacement through time for the three considered cases (at the symmetry axis, i.e.: the site of maximum deformation). All simulations begin with a quick uplift phase, which is faster and shorter for higher permeability values: the permeable system reaches ca. 33 cm of vertical displacement after 82 years, whereas the less permeable system totals 1 m of deformation in 2000 years. In the most permeable case (HO1), the vertical displacement undergoes some perturbation due to the onset of small scale convective cells which affect the distribution of pressure and temperature within the system. After a second maximum is reached (34 cm, after 468 yr), the ground level begins to subside, even if the source activity does not vary. At this time, vigorous convection

drives cold, surface water toward the deeper portion of the domain, lowering the average temperature of the system (Figure 3b). In this simulation, any excess fluids entering the system at depth are quickly discharged at the surface, and the average pore pressure does not change significantly throughout the simulation (Figure 3c). Subsidence is somewhat slower than the initial uplift, but lasts longer and it drives the ground surface ca. 50 cm below its initial elevation, where it stands to the end of the simulation. In the case with intermediate permeability, subsidence begins right after the maximum uplift (65 cm in 688 yr) is reached. Subsidence is much slower than the uplift, and by the end of the simulation the ground level is still ca. 27 cm above its initial elevation. In this case, the system undergoes a minor pressure perturbation that is quickly relieved: the residual displacement at the steady state is due to the very slow temperature decay that maintains the system hotter than the initial conditions throughout the simulation (Figure 3b). In the low-permeability case (HO3), permeability is sufficiently low that the system never relaxes: convective cells, which lower the system temperature in the other cases do not occur. Pore pressure increases significantly and is not relieved by surface discharge. As a result, no subsidence takes place and the ground level at steady state is still more than 1 m above the initial level. Comparison between the three displacement curves and the corresponding values of average pressure and temperature in the system suggest that the timing of ground displacement, over the long term, is mostly controlled by the system temperature and induced thermal expansion [*Hurwitz et al.*, 2007; *Hutnak et al.*, 2009].

Interesting insights derive from the analysis of the radial pattern of vertical displacement. Figure 4a compares the radial profile of ground uplift at the time of maximum deformation for the three simulations. In all cases, the uplift is maximum at the symme-

try axis and decays radially, resembling the profile expected for a small spherical source [*Mogi*, 1958]. Only in the most permeable case (HO1) is this profile disturbed by shallow convective cells near the symmetry axis. The radial extent of the uplifted area is largest for the less permeable domain, and reflects the size of the hot plume, which is significantly different in the three cases, although produced by the same fluid source at depth. Even at the time of maximum uplift some subsidence takes place at some distance from the symmetry axis, both for the maximum and for the minimum permeability. Subsidence (negative uplift) reflects the degree of cooling which takes place as the convection draws the cold, shallow water deeper into the system. Figure 4 also compares the radial distribution of ground displacement after 1000 years (Figure 4b), and at the end of the simulation (Figure 4c). Maximum uplift declines with time, and deformation spreads over a wider area, as the system relaxes. In the case of high permeability, most of the deformation is associated with subsidence, which increases as the average temperature declines through time.

The calculated deformations refer to the case of hot gases entering an initially cold and unperturbed system. However, active volcanoes such as Campi Flegrei usually have an active hydrothermal system, characterized by high temperatures and large gas fractions [*Chiodini et al.*, 2001]. Our monitoring network must therefore capture signals generated in a system that is already hot and more capable of adjusting to pressure changes than a liquid-dominated system.

5. Heterogeneous systems

Figure 1 illustrates the heterogeneous domain utilized for these simulations. The different rock domains are characterized by specific rock properties (Table 3). In all cases, the

permeability is higher along the vertical channel and at shallower depth. The three simulations presented below differ in the permeability assigned to each rock domain (Table 4): the first case (HE1) is the most permeable; in the second case (HE2), the permeability in each rock domain is one order of magnitude lower than in HE1; while the third case (HE3) maintains the same permeability values assigned to HE2, but with no transition zone and with a wider permeable channel that extends to a radius of 500 m. As in the homogeneous case, the initial conditions are obtained for each domain by simulating a long-lasting injection of hot fluids, according to the flow rate and composition specified in Table 1 for the quiet phase. Remarkable differences characterize the steady state attained in the three cases, reflecting the different distribution of rock permeability. Figure 5 compares the steady state distribution of temperature and gas fraction obtained with the different permeability distributions. The intermediate-permeability homogeneous case (HO2) described above is also shown for comparison. In the more permeable case (HE1), fluids quickly ascend through the permeable channel and form a thin two-phase plume that is similar to that obtained with the most permeable, homogeneous domain (HO1, Figure 2a). In this case, however, the lower permeability of the transition zone (Figure 1) confines the flow within the channel, which thus is heated more efficiently. Dry gas forms not only at shallow depths and near the fluid source, as in HO1 and HO2, but extends throughout the channel. Due to the high permeability along the channel, injected fluids ascend quickly toward the surface, while the less permeable transition zone inhibits the recharge of liquid waters from the surrounding region. As a consequence, the gas fraction within the channel remains high and convection takes place only within the shallow, more permeable layer.

When the permeability is lower (HE2), we still observe preferential heating along the vertical channel and the development of a two-phase plume with a shallow dry-gas region. As seen for the homogeneous case, when permeabilities are relatively low, convective cells do not form. The heating due to fluid injection is not compensated by downwelling of cold, shallow waters. The system evolution is much slower, but heating progressively involves a wider portion of the domain, extending to the entire transition zone. The two-phase region is thus much wider than in case HE1, and some gas evolves at depth even within the horizontal layers. The overall gas fraction is lower, with respect to the homogeneous case, and the shallow dry-gas region is thinner and wider. Some pressure build-up occurs in the deepest portion of the domain, near the source region.

The third heterogeneous case (HE3) is characterized by a wider central channel with the same permeability as the homogeneous case. The two-phase plume is hotter, dryer, and slightly less pressurized than in the homogeneous system. The high permeability within the vertical channel concentrates the source effects, favoring hotter temperatures. At the same time, the less permeable surroundings inhibit the recharge of cold water. As a result, the dry-gas region at steady state occupies most of the channel.

To examine the effects of a pulsating source of fluids on a hot system, the steady state conditions achieved above are taken as initial conditions, and a sequence of unrest and quiet periods are simulated. The case with intermediate homogeneous permeability (HO2) is taken here as the reference case. The temporal evolution of the observables described above is calculated and then compared with results for heterogeneous systems.

6. Sequence of unrest

Each unrest event is simulated as a period of increased activity of the fluid source at depth, during which both the flow rate and the relative CO_2 content are increased, as discussed in *Chiodini et al.* [2003]. We compare the response of different heterogeneous systems to the same sequence of unrest events, shown in Table 1 and described in *Todesco and Berrino* [2005] for a homogeneous domain. The system response is evaluated based on the evolution of the three observable parameters introduced above: the composition of the gas in the dry-gas region, gravity changes, and vertical ground displacement.

6.1. Gas composition

Figure 6 shows the temporal evolution of gas composition, expressed as the average CO_2/H_2O molar ratio. Shaded areas in the figure indicate unrest periods. The temporal evolution of this observable depends on the source properties and distance from the "sampling" point, but also on the initial composition of the gas phase within the system, and on unrest duration [*Chiodini et al.*, 2003; *Todesco and Berrino*, 2005; *Todesco*, 2009]. In all the simulations presented below, each unrest event increases the CO_2/H_2O molar ratio of the shallow single-phase gas region, whose composition is taken here as a proxy of fumarole composition. The four simulations are characterized by a very different behavior of this parameter. The evolution in the homogeneous case (HO2, Figure 6a) is fully described in *Todesco and Berrino* [2005]. The highest CO_2/H_2O molar ratio is reached after the first and longest unrest. Maximum CO_2 enrichment is attained only after the unrest is over. After the peak, the molar ratio declines, at a slightly slower rate. Subsequent peaks are progressively less enriched in CO_2. The minimum value reached between subsequent peaks depends on the length of the quiet period. Over the entire simulation,

the unrest periods become progressively shorter, and the overall range of compositional variation becomes narrower and characterized by smoother variations. In this simulation the composition observed at the surface never corresponds to the composition injected by the source at depth (0.17 during the quiet and 0.40 during unrest).

The first heterogeneous configuration (HE1) is characterized by the highest permeability. Compositional changes at the source are quickly transferred to the surface causing fast compositional variation (Figure 6b). In this case, the maximum molar ratio during the unrest reflects the source composition (0.4), as little dilution affects the injected fluids before they reach the surface. The peak values are reached during each crisis, shortly after the beginning of each unrest. After each peak, the molar ratio may decline slightly but only after the end of the crisis does the CO_2 content drop down substantially, below pre-crisis values. The CO_2/H_2O ratio falls somewhat below the composition of the source during quiet periods, reflecting the presence of large amounts of water vapor that form by vaporization of liquid water that reaches the hotter, axial channel from distal regions of the system. Vigorous convection takes place in this case even during quiet periods. When the unrest is over, pore pressure in the axial region decreases and this drives a radial inflow of fluid from the transition region, especially at shallow depths where the permeability is higher. As these fluids enter the permeable channel, they flow upwards and reach the dry-gas region. As a result, the two-phase plume tends to shrink a little, but significant amounts of CO_2 are driven to the dry-gas region, where they can increase CO_2 content even during the quiet periods. This re-distribution of the fluid components adds to the effects of subsequent unrest events, and contributes to the very high CO_2 enrichments. In this case, the duration of the unrest does not affect the maximum molar ratio: even the

shortest unrest yields similar enrichments, and the maximum value is achieved during the second unrest event.

The compositional trends characterizing the second heterogeneous simulation (HE2) are somewhat similar to the homogeneous case (HO2). The rate at which gas composition changes is largely controlled by the permeability of the central channel, which in this case is the same as in the homogeneous case. The presence of the less permeable transition zone focuses the flow within the channel and leads to greater CO_2 enrichments with respect to the HO2 case. Fluid circulation is not as vigorous as in the HE1 case; the dilution of CO_2-enriched fluids associated with convection is limited, and leads to smaller declines during the quiet periods. As a result, gas composition never returns to pre-crisis values, and the effects of subsequent unrest periods cumulate through time and reach a maximum value at the third unrest. This maximum is higher than that achieved in the homogeneous system, and it is larger than some of the peaks obtained with the more permeable HE1 system. This indicates that rock permeability may interact in a complex way with gas composition.

In the third case (HE3) the permeable channel is wider and directly in contact with the less permeable horizontal layers, without a transition region in between. As described above, the dry-gas region occupies most of the channel. In this case, averaging the gas composition over the entire single-phase gas region would include both the composition at the source and at the sampling point, masking the time required by the fluids to migrate from the source to the surface. In the other cases, the single-phase gas zone only developed near the surface and represented a good proxy for fumarole composition. In this case, to obtain a near-surface gas composition, we averaged the CO_2/H_2O ratio over

the upper half of the dry-gas zone. Although the rock permeability above the fluid source is similar to the HO2 and HE2 cases, rock properties in this case determine a particular phase distribution that significantly affects the system response to the simulated sequence of unrest and quiet. The absence of a liquid phase within the central channel ensures a quicker response of the system to the changes in the feeding source. The CO_2 enrichment is faster with respect to the homogenous and the HE2 cases, and the maximum CO_2/H_2O ratio is reached shortly after the end of each unrest. The first peak, which follows the longest unrest period, reaches the same CO_2 enrichment (0.4) as the feeding source during the unrest. The post-unrest system reaction is also relatively fast. The CO_2/H_2O ratio rapidly declines to the value that characterizes the feeding source during the quiet periods.

6.2. Gravity changes

The temporal variation of surface gravity at the symmetry axis is computed according to equation 1 and is plotted in Figure 7, for all the four cases considered. All simulations generate measurable gravity changes, but each case shows a very different temporal evolution and range of variation.

Gravity evolution for the homogeneous case is described in Figure 7a. Each unrest period increases the gravitational attraction: larger amounts of fluids enter the system during these periods, and pressure build-up leads to higher fluid densities. When the system relaxes during the quiet, the gravity drops, due to decompression and the upward migration of the gas-enriched fluids injected during the crises. As the simulation proceeds, the gas fraction increases and the two-phase zone progressively enlarges upwards. When the widening of the two-phase zone reaches the surface, the system is more capable of accommodating pressure transients without displacing liquid water. As a result, further

unrest events only have minor effects on gravity. The homogeneous case is described with more detail in *Todesco and Berrino* [2005].

The first heterogeneous system (HE1) is characterized by a rather complex gravity evolution associated with its very fast dynamics (Figure 7b). The beginning of each unrest period is signaled by a small, short-lasting peak that is immediately followed by a fast and large gravity drop. As in the homogeneous case, the positive gravity change reflects the addition of fluid, as the unrest begins. In this case, however, the permeability of the central channel is high enough to ensure a prompt system adjustment to the new conditions: the newly injected gases quickly propagate toward the surface, thereby increasing the average gas fraction within the system and causing an overall decline in gravity. When the unrest is over, vigorous convection persists, and drives large amounts of liquid water from the transition zone toward the central channel, causing a marked increase of gravity during the quiet period. This results in a wide range of gravity changes between subsequent unrests. At later times, the overall effect of subsequent crises is to promote convection and movement of liquid water toward the central channel, whereas the excess gas injected during each unrest is quickly discharged at the surface. As a result, the long term trend defined by gravity is positive, while the short-term variations become progressively smaller.

In the second heterogeneous case (HE2), the evolution of gravity is controlled by the lower permeability of the system, which causes widespread pressure build-up during unrest and hinders decompression during quiet periods (Figure 7c). The resulting long-term trend is characterized by slow increment and a narrow range of variation.

The gravity evolution associated with the third heterogeneous case (HE3) is broadly similar to the homogeneous case, being characterized by a long-term declining trend,

interrupted by sharp increments corresponding to the unrest events (Figure 7d). As discussed previously, changes associated with the simulated sequence of unrest events are concentrated in the central channel. Pressure and temperature variations, and associated changes in fluid density, propagate from the fluid source upwards, with only minor diffusion in the radial direction. This emphasizes the gravity changes computed at the surface. In addition, the permeable channel is dominated by the gas phase, which is highly sensitive to pressure perturbation and reacts to the changes in the system conditions. Because of these features, this system exhibits greater gravity changes than the homogeneous case.

During the simulated system evolution, gravity changes not only through time, but also through space: the sequence of unrest and quiet affects the size and shape of the two-phase plume, and this affects the value of gravity at different distances from the symmetry axis. Figure 8 compares the radial distribution of gravity in the four simulations at three different times. Shaded areas in the figure highlight the radial extent of the permeable vertical channel and of the less permeable transition region. At the end of the first unrest (Figure 8a), the high-permeability heterogeneous system (HE1) is the only one characterized by negative values. As discussed above, these early, negative values are associated with the very fast dynamic of this permeable system, wherein newly injected fluids quickly reach the surface, reducing the liquid fraction at shallow depths. Interestingly, the minimum gravity is reached at some distance (ca. 300 m) from the symmetry axis. The position of this minimum reflects the width of the two-phase plume, which widens as newly injected gases are added during the unrest. In simulation HE1, the two-phase plume is initially confined to the permeable channel. The effects of the first unrest propagate throughout the transition zone, and are small within the distal, horizontal layers. In all

the other cases, gravity changes at the end of the first unrest are positive and extend to a maximum distance of less than 1 km. Relative to the homogeneous case (HO2), the less permeable heterogeneous system HE2 shows only minor gravity changes, whereas the third heterogeneous case (HE3) exhibits the largest positive variation. In this case, the less permeable layers around the wide vertical channel confine the horizontal spreading of the ascending fluids and emphasize the effects on the surface gravity value. Figure 8b depicts gravity changes at the end of the first quiet period. At this time, the homogeneous (HO2) and HE3 cases have both relaxed and show negative gravity values in the axial region. In both cases, the edge of the two-phase plume is clearly marked by the presence of a local maximum. This maximum reaches positive values in the HE3 case, where the lower permeability of the horizontal layers hinders radial fluid propagation and thereby prevents effective dissipation of the pore pressure. Positive values characterize the other two cases, with slightly higher values for the more permeable system (HE1), where the inflow of liquid water to the permeable channel creates a complex pattern of fluid density and associated gravity change. Figure 8c shows the radial profiles at the end of the simulation. At this time, the three profiles are substantially different both with respect to peak values and their positions. The more permeable system (HE1) shows a major (+94 μGal) positive change, which reflects the inflow of liquid water, with a similarly large (-83 μGal) negative peak nearby associated with the enlargement of the two-phase region within the transition zone. The less permeable system (HE2) is still characterized by a very smooth profile, with positive values (+34 μGal) in the axial region, where the overpressure has not yet relaxed completely, and a minimum value (-99 μGal) at ca. 740 m from the axis associated with the enlargement of the two-phase plume, as the excess

gases injected during the unrest periods slowly propagate upwards. The homogeneous case (HO2) is characterized at this time by negative gravity changes, with a minimum value (-185 μGal) at ca. 600 m from the axis. The HE3 simulation is characterized by a similar profile, which however reaches a lower minimum (-342 μGal) at a greater distance from the axis.

6.3. Vertical ground displacement

The ground displacement is calculated according to equation 2. Its temporal variation at the symmetry axis is shown in Figure 9 for the four simulations. In all cases, uplift begins as the injection rate is increased, right at the beginning of each unrest phase, whereas subsidence reflects the lower inflow of hot fluids during quiet times. Ground deformation is driven by changes in pore pressure and temperature, and its evolution is faster for permeable systems, where perturbations propagate faster throughout the system. In the homogeneous case (HO2), the sequence of alternating uplift and subsidence closely reflects the evolution of the fluid source and the duration of the unrest and quiet periods (Figure 9a). A local maximum is reached at the end of each crisis, and is followed by slower subsidence during the quiet period. The rate of uplift is similar for the different unrest episodes, and the displacement associated with each crisis depends on its duration. The maximum uplift (ca. 8 cm) is therefore reached at the end of the first unrest period, which is the longest. Subsidence, on the contrary, becomes progressively slower for subsequent quiet periods. At the end of the simulation, the ground level is somewhat below its initial elevation because of the lower pressure and temperature in the system.

In the case of the higher-permeability heterogeneous system (HE1), both uplift and subsidence are very fast (Figure 9b). Within a few months, the excess fluid injected

during the crisis discharges at the surface, relieving the pore pressure. At the same time, the high permeability favors inflow of cold water towards the deeper parts of the system, reducing the average temperature. The maximum uplift is therefore reached early in the unrest and subsidence begins before the end of the unrest. At the end of the crisis, the pore pressure drops, driving sudden subsidence that brings the ground level below its original elevation. After a minimum value is reached, a few months after the beginning of the quiet period, pressure and temperature slowly adjust to the new source conditions and the ground level slowly rises again. Because the ground level does not return to its initial value before the onset of a new crisis, the effects of repeated events cumulate and maximum uplift (12 cm) is attained during the third unrest event.

The second heterogenous system (HE2) is the least permeable and shows the smallest changes in vertical ground displacement (Figure 9c). Temperature and pore pressure increase significantly, but these changes propagate very slowly from the source region. As a result, only minor deformation is observed at the surface during both the unrest and quiet phases. The low permeability does not allow effective decompression of the system during the quiet and hinders circulation of cold water from the shallow periphery of the system. As a result, the HE2 domain remains pressurized and heated even during quiet periods, and only minor subsidence is recorded at the surface. Repeated unrest events result in a progressive increase in ground elevation, which reaches its maximum value after the third crisis (7.4 cm after 136 months).

The third heterogeneous case (HE3) shows the largest deformation (Figure 9d). As in the homogeneous case (HO2), the maximum uplift (17 cm) is reached at the end of the first, longest unrest, while subsequent crises are characterized by less deformation. The

subsidence during quiet times reverses the deformation and brings the ground elevation below its initial value. In this case, the presence of less permeable horizontal layers only 500 m from the axis focuses the effects of unrest and quiet periods within the permeable channel, emphasizing the influence of pressure and temperature changes. Pressure and temperature perturbation can effectively propagate to shallow depths but remain concentrated within the axial region, enhancing ground deformation.

The radial distribution of ground displacement at different times also reveals interesting differences among the various cases considered. Figure 10a compares the radial distribution of vertical displacement at the end of the first unrest period. In all cases, the maximum uplift is located at the symmetry axis and deformation declines with radial distance, defining a profile similar to that one expected for a small spherical source. As pointed out in Figure 9, the maximum uplift is attained in the HE3 case, whereas the minimum deformation is associated with the less permeable HE2 domain. In the homogeneous case (HO2), the ground displacement reaches an intermediate value which, however, is maintained over a wide area. In the heterogeneous cases most of the deformation is accomplished within the central portion of the domain. In all cases the uplift decreases below 1 cm, within the first 3.5 km of radial distance. At the end of the first quiet period (Figure 10b), deformation is still positive (uplift) for all the simulations, but differences among the various cases emerge. Pressure and temperature perturbations are not easily dissipated in the low-permeability HE2 case. As a result, the maximum uplift diminishes, but the radial profile of vertical displacement does not change significantly with respect to the end of the first unrest period. The permeable HE1 system is characterized by a rather complex pattern of deformation, which involves a maximum value at the symmetry axis,

a minimum value inside the transition region, and some uplift outside the transition region. This pattern reflects the different behavior of fluid circulation within different rock domains. The homogeneous and HE3 case are characterized by similar patterns, with maximum displacement localized at the edge of the two-phase plume. The low permeability of the horizontal layers in the HE3 simulation confines the fluid circulation within the central channel and accentuates the decompression associated with the quiet period. At the end of the simulation (Figure 10c), after four unrest and four quiet periods, the HE2 case is still characterized by the largest amount of uplift, but the radial profile now reflects the presence of the permeable channel and the intermediate transition region. In the more permeable HE1 case, the differences among different domains are larger, and maximum uplift is recorded within the transition region. Both the HO2 and the HE2 cases are characterized by some degree of subsidence, which is larger for the heterogeneous domain. In both cases, a local maximum indicates the edge of the two-phase plume.

7. Discussion and Conclusion

In this work we discuss the influence of permeability structure on the evolution of a shallow hydrothermal system fed by magmatic fluids. Starting from the simple conceptual model developed for the Campi Flegrei caldera [*Chiodini et al.*, 2003], we first compared the steady state conditions achieved with different choices of rock permeability, given the same, stationary fluid source at depth. We then studied the effects of periodic unrest events, simulated as periods of increased source activity (in terms of flow rate and CO_2 content). The same sequence of unrest and quiet periods was simulated both for homogeneous and for heterogeneous systems, in which different rock domains are characterized by different rock permeabilities. Although we do not perform a direct comparison with

603 the data from the Campi Flegrei caldera, the rock properties and the spatial distribution
604 of rock types are consistent with available knowledge of the caldera settings [*Rosi and*
605 *Sbrana*, 1987; *Orsi et al.*, 1996; *Vanorio et al.*, 2002; *Acocella*, 2008]. The range of values
606 and the spatial distribution of permeability strongly affect the values achieved by state
607 variables under given boundary conditions. When boundary conditions change (as when
608 an unrest event is simulated), rock properties control the system's reaction time, the rate
609 at which system conditions evolve and the time at which they adjust to the new bound-
610 ary conditions. Hydraulic properties also determine the fraction of the system volume
611 that is affected by the changes, that is the system's sensitivity to external perturbations.
612 High permeability above the fluid source at depth favors the development of a thin, gas-
613 rich plume which quickly reacts to changes in source activity. Wider plumes develop in
614 less permeable systems, which are characterized by a slower evolution and by lower gas
615 fraction. Low permeability favors heating and pressure build-up near the source region.
616 When a permeable channelway is present in the axial region, and surrounded by less per-
617 meable horizontal layers, the effects of source changes are confined within the channel
618 and accentuated, while exchange of heat and fluids with the distal region of the domain
619 is hindered.

620 These differences in system conditions translate into very different behavior of param-
621 eters that can be monitored at the surface. The signals that we record there result from
622 complex interaction between degassing magma at depth, the host rock through which
623 the fluids circulate, and the shallow waters that may permeate the rocks. The value
624 and distribution of rock permeability affect the efficiency of the heat and mass transfer
625 from the deeper region of the volcano toward the surface, control the degree of mixing

among different fluid phases, and influence the occurrence of chemical reactions between the fluids and between the fluids and the solid rocks [*Todesco*, 2008, and ref. therein]. A comparison between the variability of gas composition and gravity after an unrest period showed previously that gravity changes are more sensitive to source properties than gas composition [*Todesco*, 2009]. The simulations presented here show that the variability of gas composition is controlled by permeability (being higher for larger permeability values), and that compositional changes are accentuated when fluids are channeled along a permeable zone surrounded by less permeable domains. When all rock domains are relatively permeable (HE1) compositional changes record a very fast reaction to source changes, but also a complex interaction with distal, water-rich fluids that can easily propagate toward the axial region during the quiet. The resulting trend of gas composition is characterized by local minima and maxima which occur during both the unrest and the quiet phases. When rock domains have a lower permeability (HE2), the system reaction speed is reduced. Less vigorous convection hinders the propagation of the CO_2-rich fluids injected during the unrest. As a result, the effects of subsequent crises accumulate through time and lead to higher CO_2 enrichments. When a wider permeable channel is confined by less permeable rocks (HE3), fluids propagate through the channel and reach the surface with little dilution during the unrest. During the quiet period, fluid convection within the channel allows for an effective mitigation of the unrest effects, and gas composition tends to return to its initial value. The other two observables (gravity change and vertical displacement) follow similar trends: more complicated for the more permeable system; slower, with a progressive accumulation of the (minor) effects of subsequent unrests, for the less permeable system; similar to the homogeneous case, but with enhanced effects, in

649 the third heterogeneous case examined. In our simulations, the inflow of external waters
650 in the permeable system modifies the signals generated during and after a crisis. All the
651 porous rock is water saturated and therefore the availability of external water may be
652 overestimated with respect to a real system. Nevertheless, the importance of this con-
653 tribution (both from the thermal and compositional point of view) suggests the need to
654 better define of the amount of shallow water entering fumarolic conduits in real systems.

655 The three parameters (gas composition, gravity, and uplift) which are characterized
656 by different temporal evolutions, are affected in a similar way by the permeability dis-
657 tribution. At present, given a time series of an observable parameter, it is not possible
658 to filter out the influence of the porous medium. Our simulations suggest that it may
659 be important, and particular care should be taken as we try to infer the properties and
660 conditions of the magmatic source from data collected at the surface. Although these sim-
661 ulations are performed assuming no changes in rock properties through time, our results
662 imply that fracturing or self-sealing processes could potentially lead to large changes in
663 the observable parameters, even if the deep source remains unchanged. In this case, the
664 departure of monitored signals from their baseline values (i.e., the apparent unrest) would
665 not reflect the state of the magmatic system at depth, but rather the evolution of the
666 shallower portion of the volcanic edifice. This once again invites us to use great caution
667 while deciphering the meaning of unrest events.

668 **Acknowledgments.** This work was carried out within the research project V1 - UN-
669 REST, founded by the Italian Civil Protection Department. The manuscript was greatly
670 improved by accurate reviews carried out by Steven Ingebritse, Nicolas Fournier and Luca
671 Crescentini.

References

Acocella, V. (2008), Activating and reactivating pairs of nested collapses during caldera-forming eruptions: Campi Flegrei (Italy), *Geophys. Res. Lett.*, *35*(17), 1–5.

Allard, P., A. Maiorani, D. Tedesco, G. Cortecci, and B. Turi (1991), Isotopic study of the origin of sulfur and carbon in Solfatara fumaroles, Campi Flegrei caldera, *J. Volcanol. Geotherm. Res.*, *48*(1-2), 139–159.

Amoruso, A., L. Crescentini, A. T. Linde, I. S. Sacks, R. Scarpa, and P. Romano (2007), A horizontal crack in a layered structure satisfies deformation for the 2004–2006 uplift of Campi Flegrei, *Geophys. Res. Lett.*, *34*(L22313), doi:10.1029/2007GL031644.

Amoruso, A., L. Crescentini, and G. Berrino (2008), Simultaneous inversion of deformation and gravity changes in a horizontally layered half-space: Evidences for magma intrusion during 1982-1984 unrest at Campi Flegrei caldera (Italy), *Earth Planet. Sci. Lett.*, *272*, 181–188, doi:10.1016/j.epsl.2008.04.040.

Barberi, F., G. Corrado, F. Innocenti, and G. Luongo (1984), Phlegrean Fields 1982 – 1984: Brief chronicle of a volcano emergency in a densely populated area, *Bull. Volcanol.*, *47*, 175–185.

Battaglia, M., C. Troise, F. Obrizzo, F. Pingue, and G. De Natale (2006), Evidence for fluid migration as the source of deformation at Campi Flegrei caldera (Italy), *grl*, *33*, L01307, doi:10.1029/2005GL024904.

Berrino, G., G. Corrado, G. Luongo, and B. Toro (1984), Ground deformation and gravity changes accompanying the 1982 Pozzuoli uplift, *Bull. Volcanol.*, *47*, 188–200.

Bodnar, R. J., C. Cannatelli, B. De Vivo, A. Lima, H. E. Belkin, and A. Milia (2007), Quantitative model for magma degassing and ground deformation (bradyseism) at

694 Campi Flegrei, Italy: Implications for future eruptions, *Geology*, *35*(9), 791–794.

695 Bruno, P. P. G., G. P. Ricciardi, Z. Petrillo, V. Di Fiore, A. Troiano, and G. Chiodini
696 (2007), Geophysical and hydrogeological experiments from a shallow hydrothermal sys-
697 tem at Solfatara Volcano, Campi Flegrei, Italy: Response to caldera unrest, *J. Geophys.*
698 *Res.*, *112*(B06201), doi:10.1029/2006JB004383.

699 Casertano, L., A. Oliveri del Castillo, and M. T. Quagliariello (1976), Hydrodynamics
700 and geodynamics in the Phlegrean Fields area of Italy, *Nature*, *264*, 161–164.

701 Chiarabba, C., and M. Moretti (2006), An insight into the unrest phenomena at the
702 Campi Flegrei caldera from Vp and Vp/Vs tomography, *Terra Nova*, *18*, 373–379.

703 Chiodini, G. (2009), CO_2/CH_4 ratio in fumaroles a powerful tool to detect magma
704 degassing episodes at quiescent volcanoes, *Geophys. Res. Lett.*, *36*(L02302), doi:
705 10.1029/2008GL036347.

706 Chiodini, G., F. Frondini, C. Cardellini, D. Granieri, L. Marini, and G. Ventura (2001),
707 CO_2 degassing and energy realease at Solfatara volcano, Campi Flegrei, Italy, *J. Geo-*
708 *phys. Res.*, *106*(16), 16,213–16,221.

709 Chiodini, G., M. Todesco, S. Caliro, C. Del Gaudio, G. Macedonio, and M. Russo (2003),
710 Magma degassing as a trigger of bradyseismic events: The case of Phlegrean Fields
711 (Italy), *Geophys. Res. Lett.*, *30*(8), 1434–1437.

712 Chiodini, G., S. Caliro, C. Cardellini, D. Granieri, R. Avino, A. Baldini, M. Donnini, and
713 C. Minopoli (2009), Long term variations of the Campi Flegrei (Italy) volcanic system
714 as revealed by the monitoring of hydrothermal activity, *J. Geophys. Res.*, in press.

715 Corey, A. (1954), The interrelation between gas and oil relative permeabilities, *Producers*
716 *Monthly*, *19*(1), 38–41.

717 Crescentini, L., and A. Amoruso (2007), Effects of crustal layering on the inversion of
718 deformation and gravity data in volcanic areas: An application to the Campi Flegrei
719 caldera, Italy, *J. Geophys. Res.*, *34*(L09303), doi:10.1029/2007GL029919.

720 De Natale, G., F. Pingue, P. Allard, and A. Zollo (1991), Geophysical and geochemical
721 modelling of the 1982-1984 unrest phenomena at Campi Flegrei caldera (Southern Italy),
722 *J. Volcanol. Geotherm. Res.*, *48*, 199–222.

723 De Natale, G., C. Troise, and F. Pingue (2001), A mechanical fluid-dynamical model for
724 ground movements at Campi Flegrei caldera, *J. Geodyn.*, *32*, 487–571.

725 Hurwitz, S., L. B. Christiansen, and P. A. Hsieh (2007), Hydrothermal fluid flow and
726 deformation in large calderas: Inferences from numerical simulations, *J. Geophys. Res.*,
727 *112*, B02206, doi:10.1029/2006JB004689.

728 Hutnak, M., S. Hurwitz, S. E. Ingebritsen, and P. A. Hsieh (2009), Numerical models
729 of caldera deformation: Effects of multiphase and multicomponent hydrothermal fluid
730 flow, *J. Geophys. Res.*, *114*, B04411, doi:10.1029/2008JB006151.

731 Ingebritsen, S., and C. Manning (2010), Permeability of the continental crust: dynamic
732 variations inferred from seismicity and metamorphism, *Geofluids*, in press.

733 Judenherc, S., and A. Zollo (2004), The Bay of Naples (southern Italy): Constraints on
734 the volcanic structures inferred from a dense seismic survey, *J. Geophys. Res.*, *109*(B10),
735 doi:10.1029/2003JB002876.

736 Lima, A., B. De Vivo, F. J. Spera, R. J. Bodnar, A. Milia, C. Nunziata, H. E. Belkin, and
737 C. Cannatelli (2009), Thermodynamic model for uplift and deflation episodes (brady-
738 seism) associated with magmatic–hydrothermal activity at the Campi Flegrei (Italy),
739 *Earth-Science Reviews*, *97*, 44–58.

740 Manning, C., and S. Ingebritsen (1999), Permeability of the continental crust: Implica-
741 tions of geothermal data and metamorphic systems, *Rev. Geophys.*, *37*(1), 127–150.
742 Mogi, K. (1958), Relations of the eruptions of various volcanoes and the deformations of
743 the ground surface around them, *Bull. Earthq. Res. Inst. Tokyo Univ.*, *36*, 99–134.
744 Newhall, C., and D. Dzurisin (1988), Historical unrest at large calderas of the world,
745 *USGS Bull.*, (1855), 1108.
746 Orsi, G., S. D. Vita, and M. Di Vito (1996), The restless, resurgent Campi Flegrei nested
747 caldera (Italy): constraints on its evolution and configuration, *J. Volcanol. Geotherm.*
748 *Res.*, *74*(3-4), 179–214.
749 Orsi, G., S. M. Petrazzuoli, and K. Wohletz (1999), Mechanical and thermo-fluid be-
750 haviour during unrest at the Campi Flegri caldera (Italy), *J. Volcanol. Geotherm. Res.*,
751 *91*, 453–470.
752 Peluso, F., and I. Arienzo (2007), Experimental determination of permeability
753 of Neapolitan Yellow Tuff, *J. Volcanol. and Geotherm. Res.*, *160*(1-2), doi:
754 10.1016/j.jvolgeores.2006.09.004.
755 Pruess, K., C. M. Oldenburg, and G. Moridis (1999), TOUGH2 user's guide, version 2.0,
756 *Paper LBNL-43134*, Lawrence Berkeley Natl. Lab., Berkeley, CA, USA.
757 Rinaldi, A. P., M. Todesco, and M. Bonafede (2010), Hydrothermal instability and ground
758 displacement at the Campi Flegrei caldera, *Phys. Earth Planet. Int.*, *178*, 155–161, doi:
759 10.1016/j.pepi.2009.09.005.
760 Rosi, M., and A. Sbrana (1987), The Phlegrean Fields, *Quaderni de La Ricerca Scientifica*,
761 *114*, Consiglio Nazionale delle Ricerche, Roma ,Italy.

762 Sorey, M., V. McConnell, and E. Roeloffs (2003), Summary of recent research in Long
763 Valley caldera, California, *J. Volcanol. Geotherm. Res.*, *127*(3-4), 165–173.
764 Tedesco, D. (1994), Chemical and isotopic gas emissions at Campi Flegrei: Evidence for
765 an aborted period of unrest, *J. Geophys. Res.*, *99*(B8), doi:doi:10.1029/94JB00465.
766 Tedesco, D., P. Allard, Y. Sano, and H. Wakita (1990), Helium-3 in subaerial and subma-
767 rine fumaroles of Campi Flegrei caldera, Italy, *Geochimica et Cosmochimica Acta*, *54*,
768 1105–1116.
769 Todesco, M. (2008), Hydrothermal fluid circulation and its effects on caldera unrest, in
770 *Caldera Volcanoes: Analysis, Modeling and Response, Dev. Volcanol.*, vol. 10, edited by
771 J. Gottsmann and J. Marti, pp. 393–416, Elsevier, Amsterdam.
772 Todesco, M. (2009), Signals from the campi flegrei hydrothermal system: Role of a "mag-
773 matic" source of fluids, *J. Geophys. Res.*, *114*, B05201, doi:10.1029/2008JB006134.
774 Todesco, M., and G. Berrino (2005), Modelling hydrothermal fluid circulation and gravity
775 signals at the Phlegrean Fields caldera, *Earth Plan. Sci. Lett.*, *240*, 328–338.
776 Todesco, M., G. Chiodini, and G. Macedonio (2003), Monitoring and modelling hydrother-
777 mal fluid emission at La Solfatara (Phlegrean Field, Italy). An interdisciplinary ap-
778 proach to the study of diffuse degassing, *J. Volcanol. Geotherm. Res.*, *125*, 57–80.
779 Todesco, M., J. Rutqvist, G. Chiodini, K. Pruess, and C. M. Oldenburg (2004), Model-
780 ing of recent volcanic episodes at Phlegrean Fields (Italy): geochemical variations and
781 ground deformation, *Geothermics*, *33*, 531–547.
782 Tramelli, A., E. Del Pezzo, F. Bianco, and E. Boschi (2006), 3D scattering image of the
783 Campi Flegrei caldera (southern Italy): New hints on the position of the old caldera
784 rim, *Phys. Earth Planet. Int.*, *155*, 269–280, doi:10.1016/j.pepi.2005.12.009.

Troise, C., G. De Natale, F. Pingue, F. Obrizzo, P. De Martino, U. Tammaro, and E. Boschi (2007), Renewed ground uplift at Campi Flegrei caldera (Italy): New insight on magmatic processes and forecast, *Geophys. Res. Lett.*, *34*(L03301).

Vanorio, T., M. Prasad, D. Patella, and A. Nur (2002), Ultrasonic velocity measurements in volcanic rocks: correlation with microtexture, *Geophys. J. Int.*, *149*(1), 22–36.

Villemant, B., G. Hammouya, A. Michel, M. Semet, J.-C. Komorowski, G. Boudon, and J.-L. Cheminée (2005), The memory of volcanic waters: Shallow magma degassing revealed by halogen monitoring in thermal springs of La Soufrière volcano (Guadeloupe, Lesser Sntilles), *Earth and Plan. Sci. Lett.*, *237*(3-4), 710–728, doi: doi:10.1016/j.epsl.2005.05.013.

Walsh, J., and J. Rice (1979), Local changes in gravity resulting from deformation, *J. Geophys. Res*, *84*(B1).

Zollo, A., N. Maercklin, M. Vassallo, D. Dello Iacono, J. Virieux, and P. Gasparini (2008), Seismic reflections reveal a massive melt layer feeding Campi Flegrei caldera, *Geophys. Res. Lett.*, *35*(12), doi:10.1029/2008GL034242.

Table 1. Source activity: mass flow rate and composition of injected fluids during unrest and quiet times. Following *Todesco and Berrino* [2005], each simulation begins with an unrest phase, and involves 4 unrest and 4 quiet periods. The unrest events last 16, 9, 8, and 3 months, respectively; the following quiet times last 42, 56, 62, and 56 months, respectively. The fluid mixture is injected into the system at constant enthalpy, corresponding to a fluid temperature of ca. 623 K

Injected fluids	Crises	Quiet
CO_2 (tons/day)	6000	1000
H_2O (tons/day)	6100	2400
Total (tons/day)	12100	3400
CO_2/H_2O (molar ratio)	0.40	0.17

Table 2. Rock properties considered in the simulation of homogeneous system (HO). Rock permeability is isotropic and, unless otherwise specified, is equal to 10^{-14} m^2.

Density	2000 kg m^{-3}
Porosity	0.20
Conductivity	2.80 W m^{-1} K^{-1}
Specific Heat	1000 J kg^{-1} K^{-1}

Table 3. Rock properties assigned to the different rock domains shown in Figure 1, in all heterogeneous simulations : ρ, rock density (kg/m^3); ϕ, porosity; W, thermal conductivity (W m^{-1} K^{-1}); C, specific heat (J kg^{-1} K^{-1}).

	ρ	ϕ	W	C
FUMAR	1800	0.10	1.15	900
TRAN1	1600	0.15	1.15	900
TRAN2	1800	0.15	1.15	900
TRAN3	2000	0.15	1.50	1000
SHALLOW	1600	0.45	1.15	900
NYT	1800	0.35	1.15	900
DEEP	2000	0.15	1.50	1000

Table 4. Values of rock permeability assigned to each rock domain in the 3 heterogeneous simulations. When two values are listed, they refer to the permeability along the horizontal and vertical directions, respectively.

	HE1	*HE2*	*HE3*
FUMAR	10^{-13}	10^{-14}	10^{-14}
TRAN1	$8 \cdot 10^{-14}$	$8 \cdot 10^{-15}$	10^{-14}
TRAN2	$5 \cdot 10^{-14}$	$5 \cdot 10^{-15}$	10^{-14}
TRAN3	10^{-14}	10^{-15}	10^{-14}
SHALLOW	$5 \cdot 10^{-14}$	$5 \cdot 10^{-15}$	$5 \cdot 10^{-15}$
NYT	10^{-14}	10^{-15}	10^{-15}
DEEP	10^{-15}	10^{-16}	10^{-16}

Table 5. Mechanical properties used to compute vertical displacement. The values reported below are used for all rock domains in all simulations, under the assumption that changes in hydraulic properties are not accompanied by changes in mechanical properties. μ is the shear modulus, K is the drained bulk modulus, K'_s is the bulk modulus of the solid constituent and α_s is the volumetric thermal expansion coefficient for the solid matrix.

μ	2 GPa
K	5 GPa
K'_s	30 GPa
α_s	10^{-5} K^{-1}

Figure 1. Detail of the axial region of the two-dimensional, axisymmetric computational domain. The domain extends radially to 10 km, and reaches a maximum depth of 1.5 km. Bottom and lateral boundaries are impervious and adiabatic, while atmospheric conditions are fixed along the top, which is open to heat and fluid flow. The source of hot, magmatic fluids is indicated in red along the bottom, near the symmetry axis. Flow rate and composition of injected fluids are listed in Table 1. Different shades identify the different rock domains used for the simulation of heterogeneous systems, with darker colors associated with lower permeability values. The rock properties used in different simulations are listed in Table 3.

Figure 2. Steady state conditions associated with a continued injection of hot fluids at the source for different values of homogeneous and isotropic permeability: (a) 10^{-13} m^2; (b) 10^{-14} m^2; (c) 10^{-15} m^2. Shaded colors indicate the volumetric gas fraction and contour lines refer to temperature (°C). The injected fluids are listed in Table 1 (quiet).

Figure 3. (a) Temporal evolution of vertical ground displacement during the evolution towards steady state for homogeneous systems with different values of rock permeability. The displacement is calculated at the top of the domain, at the symmetry axis. The corresponding evolution of average temperature and pressure (computed over the entire computational domain) are shown in (b) and (c), respectively.

Figure 4. Radial distribution of vertical ground displacement for homogeneous systems at different times: (a) when the maximum deformation is achieved; (b) after 1000 years; (c) after 10000 years of simulation.

Figure 5. Steady state conditions associated with continuous injection of hot fluids. Different plots refer to different permeability distributions within the system: (a) homogeneous case (HO2, 10^{-14} m^2); (b) heterogeneous domain HE1; (c) heterogeneous domain HE2; (d) heterogeneous domain HE3. Shaded colors indicate the volumetric gas fraction and contour lines refer to temperature (°C). The distribution of heterogeneous rock domains is shown in Figure 1, and permeability values used in the three heterogeneous simulations are listed in Table 4.

Figure 6. Temporal evolution of gas composition corresponding to the sequence of unrest and quiet periods described in Table 1. (a) Homogeneous domain (HO2); (b) heterogeneous domain HE1; (c) heterogeneous domain HE2; (d) heterogeneous domain HE3. Shaded areas indicate the timing and duration of unrest events.

Figure 7. Temporal evolution of gravity changes corresponding to the sequence of unrest and quiet periods described in Table 1. (a) Homogeneous domain (HO2); (b) heterogeneous domain HE1; (c) heterogeneous domain HE2; (d) heterogeneous domain HE3. Shaded areas indicate the timing and duration of unrest events.

Figure 8. Radial distribution of gravity changes at different times: (a) end of first unrest event; (b) end of first quiet period; (c) end of simulation. Shaded areas indicate the radial extent of the permeable channel and transition region.

Figure 9. Temporal evolution of vertical ground displacement (at the symmetry axis) corresponding to the sequence of unrest and quiet periods described in Table 1. (a) Homogeneous domain (HO2); (b) heterogeneous domain HE1; (c) heterogeneous domain HE2; (d) heterogeneous domain HE3. Shaded areas indicate the timing and duration of unrest events.

Figure 10. Radial distribution of vertical ground displacement at different times: (a) end of first unrest event; (b) end of first quiet period; (c) end of simulation. Shaded areas indicate the radial extent of the permeable channel and of the transition region. Note changes in vertical scale between (a), (b), and (c).

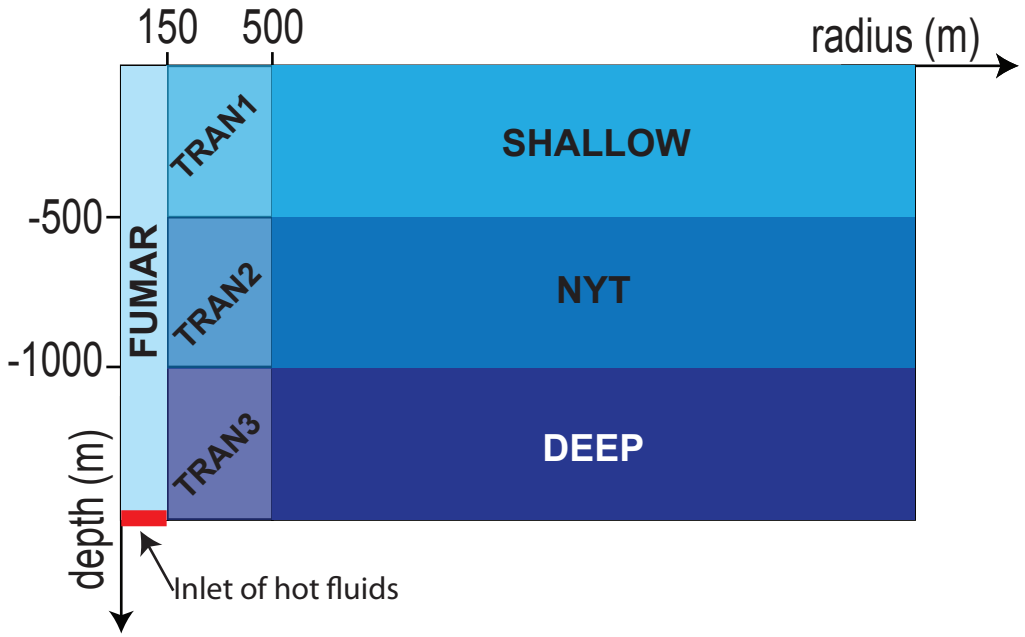
150
500
radius (m)
TRAN1
SHALLOW
-500
FUMAR
TRAN2
NYT
-1000
TRAN3
DEEP
depth (m)
Inlet of hot fluids

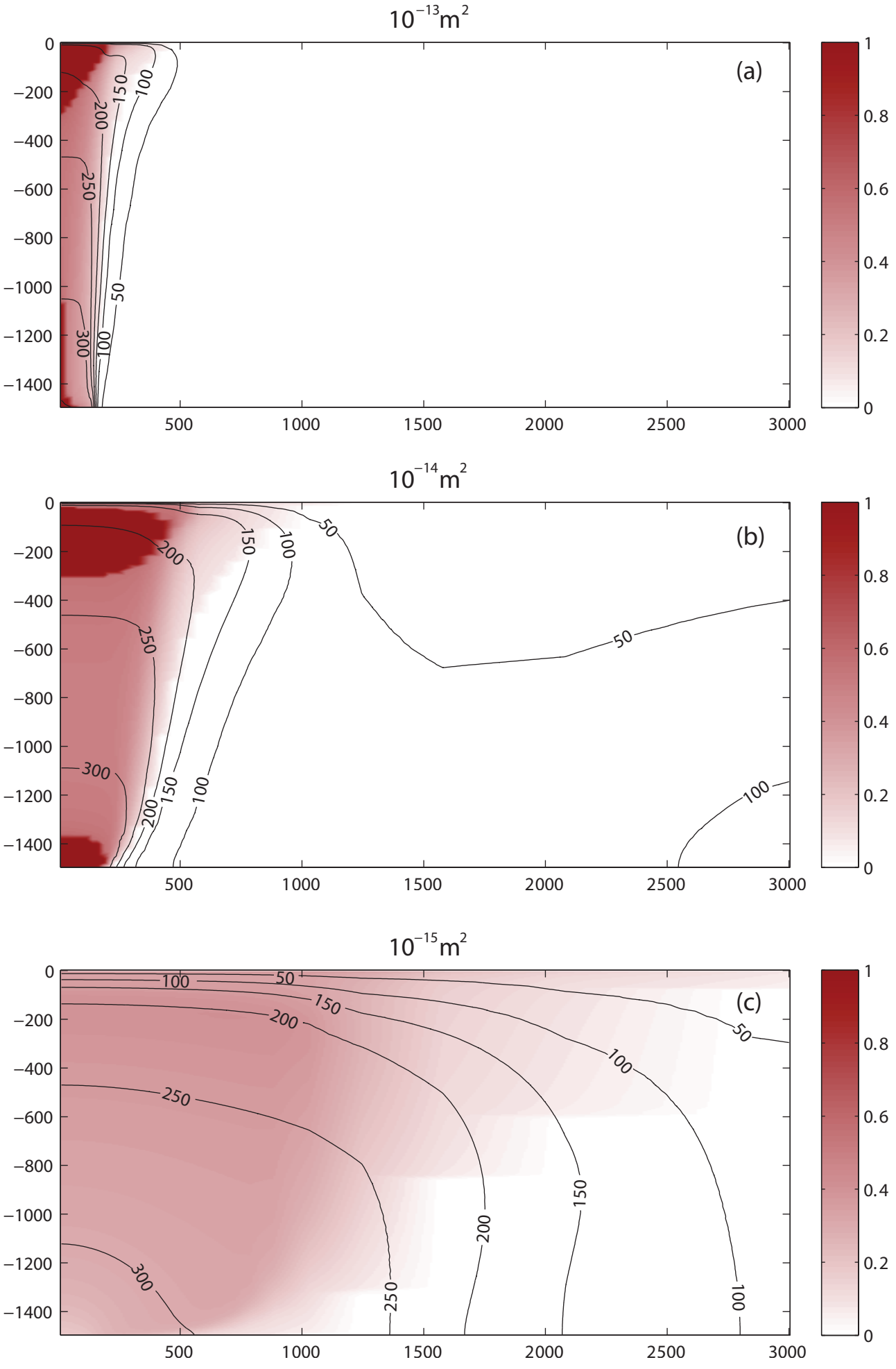
10^{-13}m^2
(a)
10^{-14}m^2
(b)
10^{-15}m^2
(c)
0
−200
−400
−600
−800
−1000
−1200
−1400
500
1000
1500
2000
2500
3000
1
0.8
0.6
0.4
0.2
0

Figure 2.

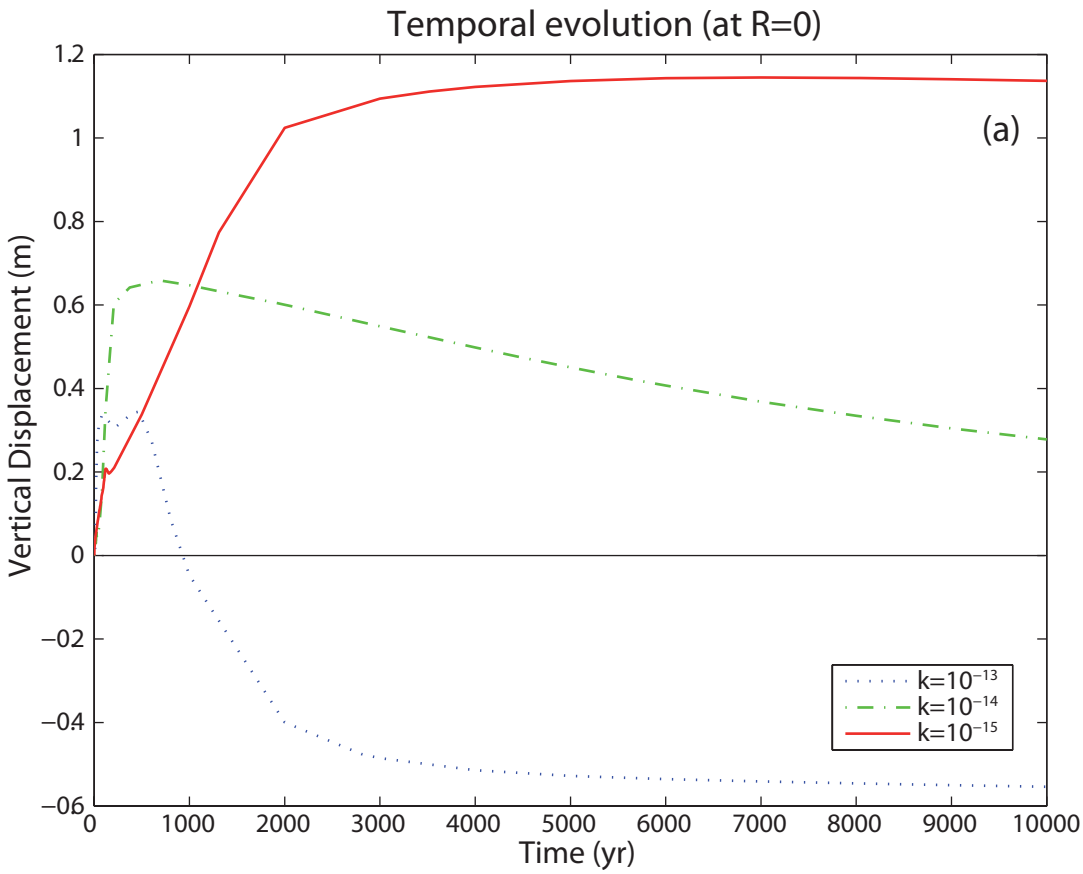
Temporal evolution (at R=0)
(a)
Vertical Displacement (m)
Time (yr)
k=10^-13
k=10^-14
k=10^-15

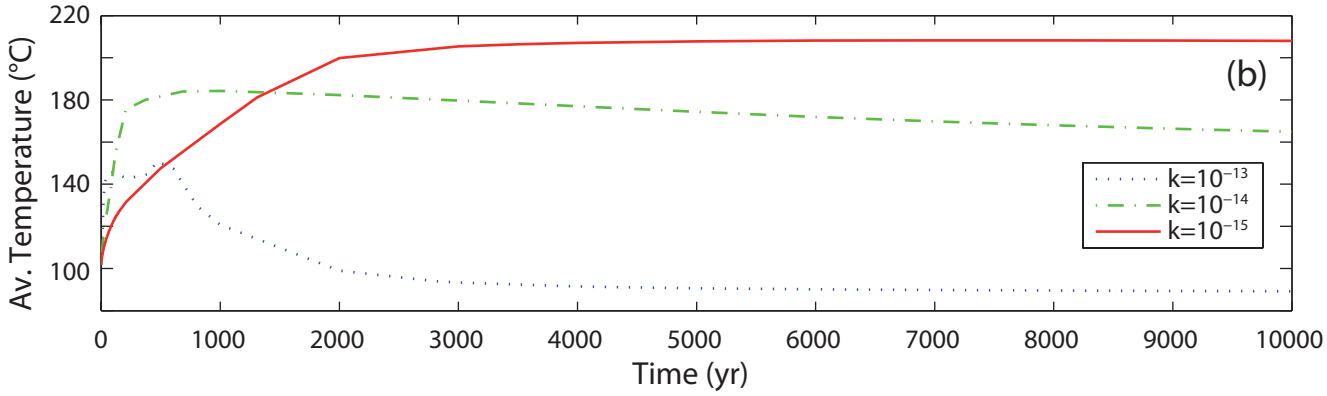
(b)
Av. Temperature (°C)
Time (yr)
k=10^-13
k=10^-14
k=10^-15

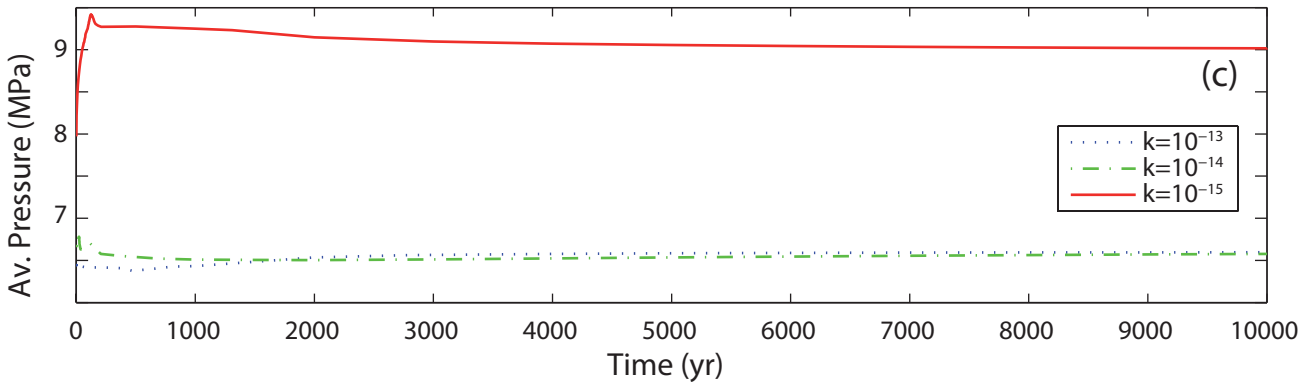
(c)
Av. Pressure (MPa)
Time (yr)
k=10^-13
k=10^-14
k=10^-15

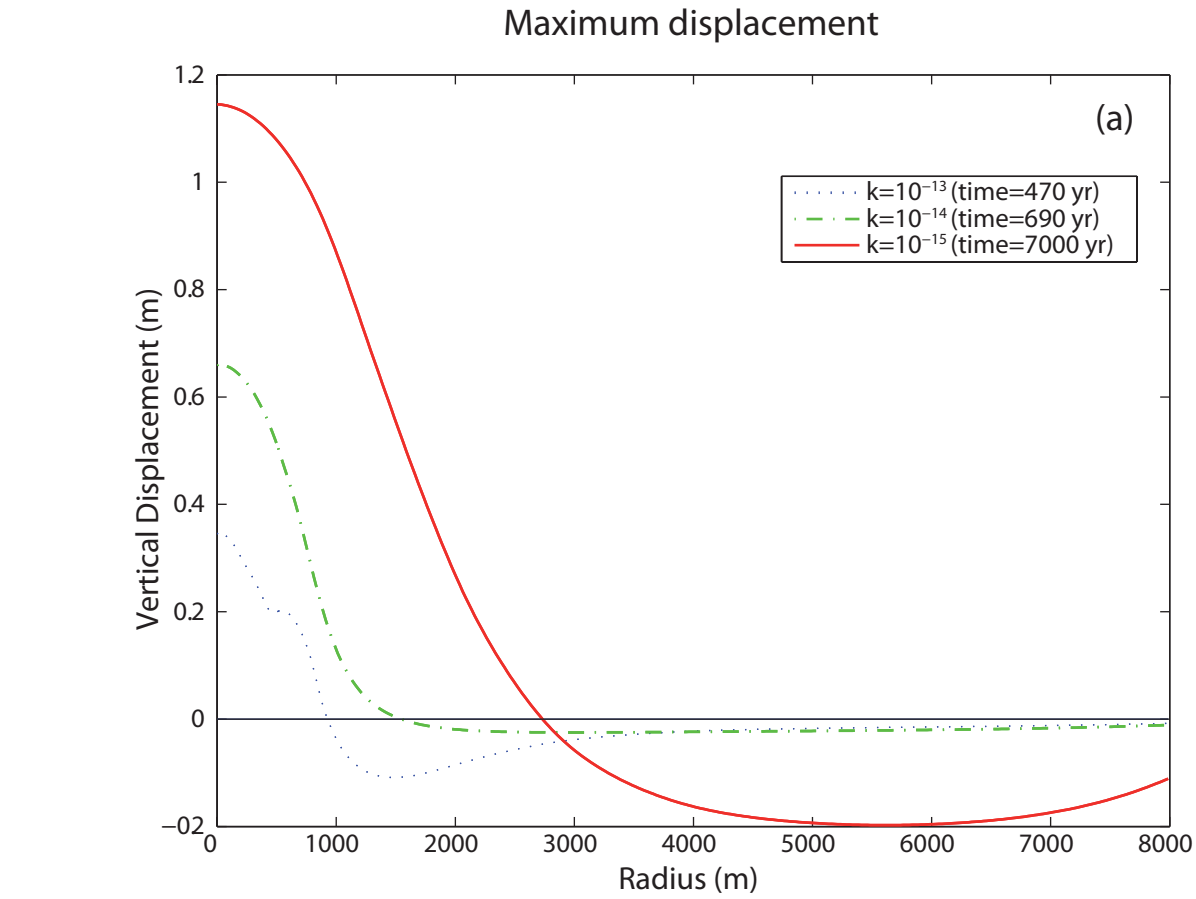
Maximum displacement
(a)
k=10−13 (time=470 yr)
k=10−14 (time=690 yr)
k=10−15 (time=7000 yr)
Vertical Displacement (m)
Radius (m)
1.2
1
0.8
0.6
0.4
0.2
0
−02
0
1000
2000
3000
4000
5000
6000
7000
8000

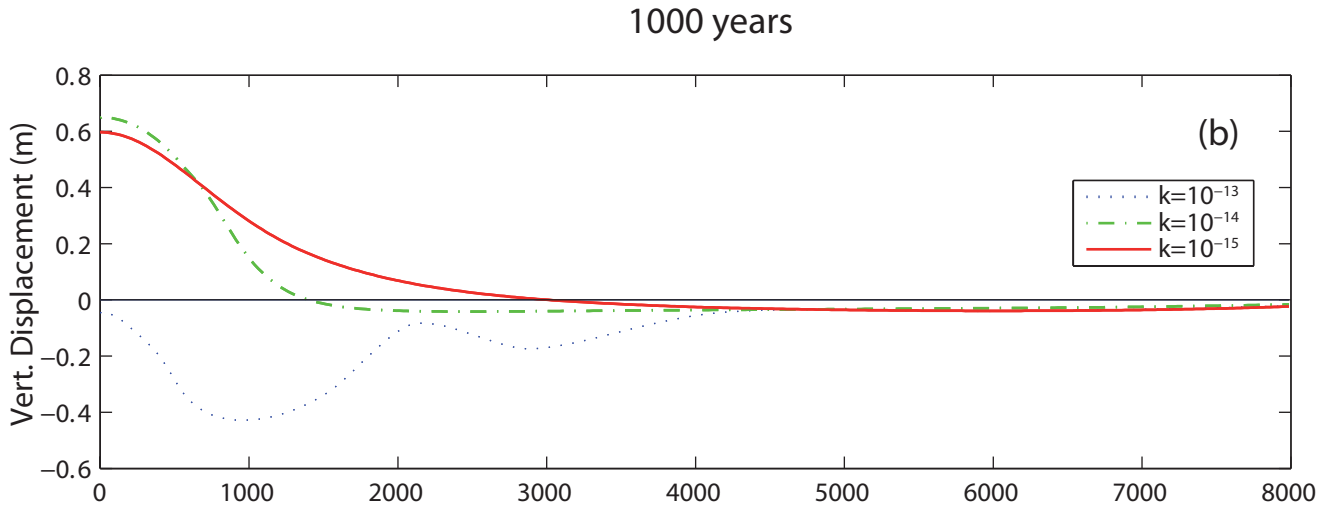
1000 years
(b)
k=10−13
k=10−14
k=10−15
Vert. Displacement (m)
0.8
0.6
0.4
0.2
0
−0.2
−0.4
−0.6
0
1000
2000
3000
4000
5000
6000
7000
8000

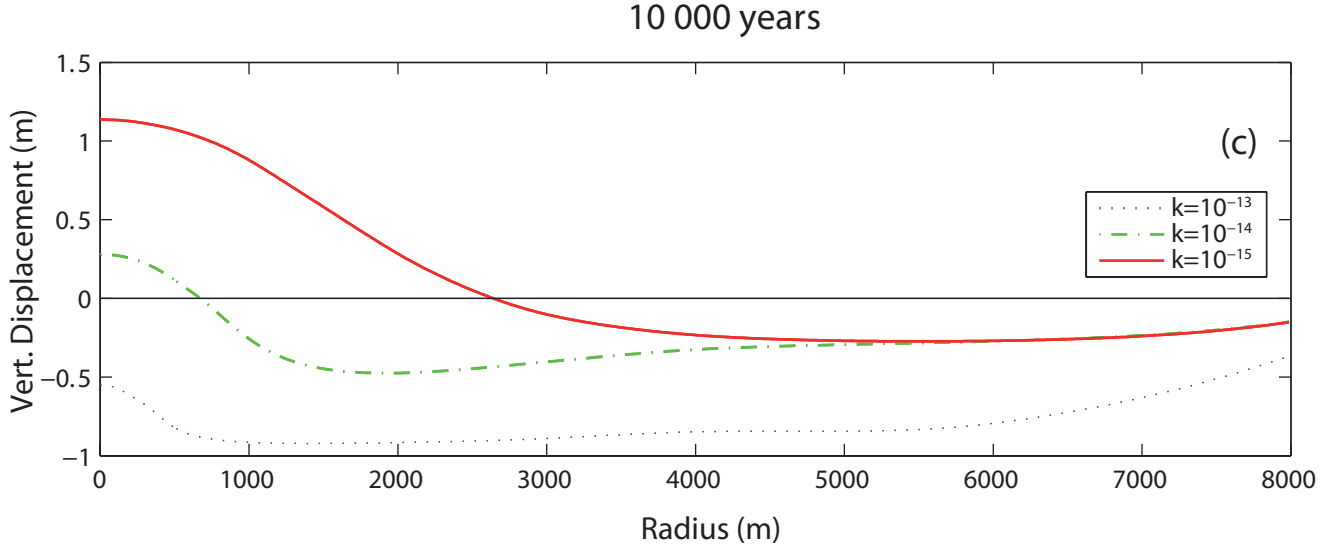
10 000 years
(c)
k=10−13
k=10−14
k=10−15
Vert. Displacement (m)
Radius (m)
1.5
1
0.5
0
−0.5
−1
0
1000
2000
3000
4000
5000
6000
7000
8000

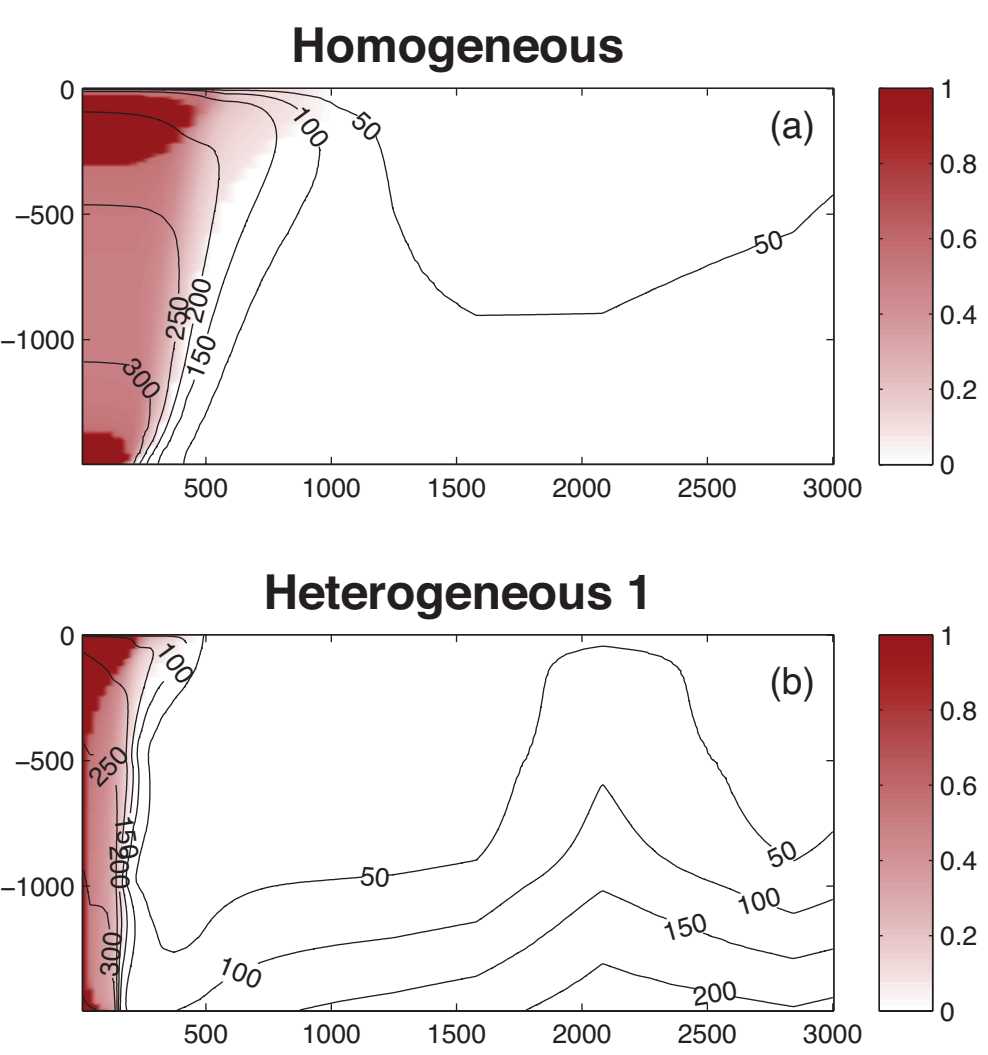
Homogeneous
(a)
0
−500
−1000
500
1000
1500
2000
2500
3000
100
50
250
200
150
300
50
1
0.8
0.6
0.4
0.2
0
Heterogeneous 1
(b)
0
−500
−1000
500
1000
1500
2000
2500
3000
100
250
150
200
300
50
100
50
150
200
1
0.8
0.6
0.4
0.2
0

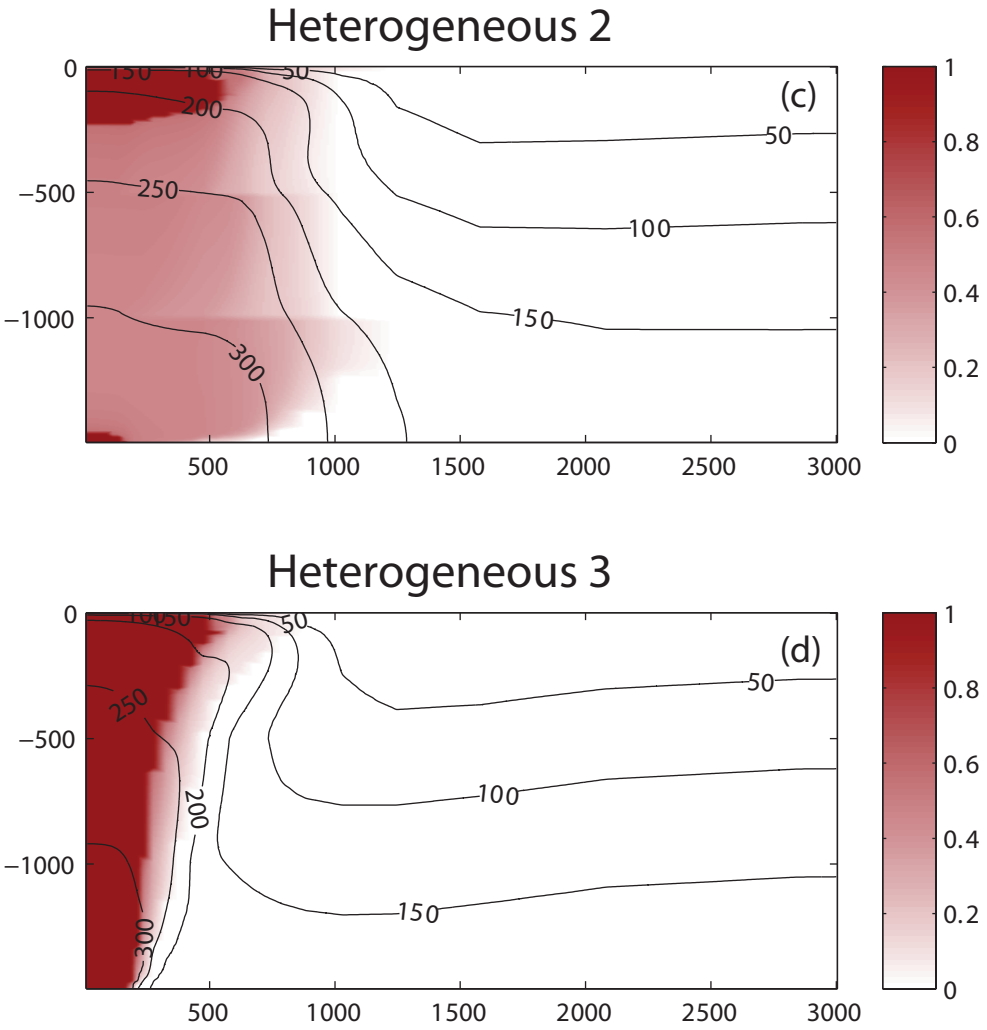
Heterogeneous 2
(c)
0
−500
−1000
500
1000
1500
2000
2500
3000
50
100
150
200
250
300
1
0.8
0.6
0.4
0.2
0
Heterogeneous 3
(d)
0
−500
−1000
500
1000
1500
2000
2500
3000
50
100
150
200
250
300
1
0.8
0.6
0.4
0.2
0

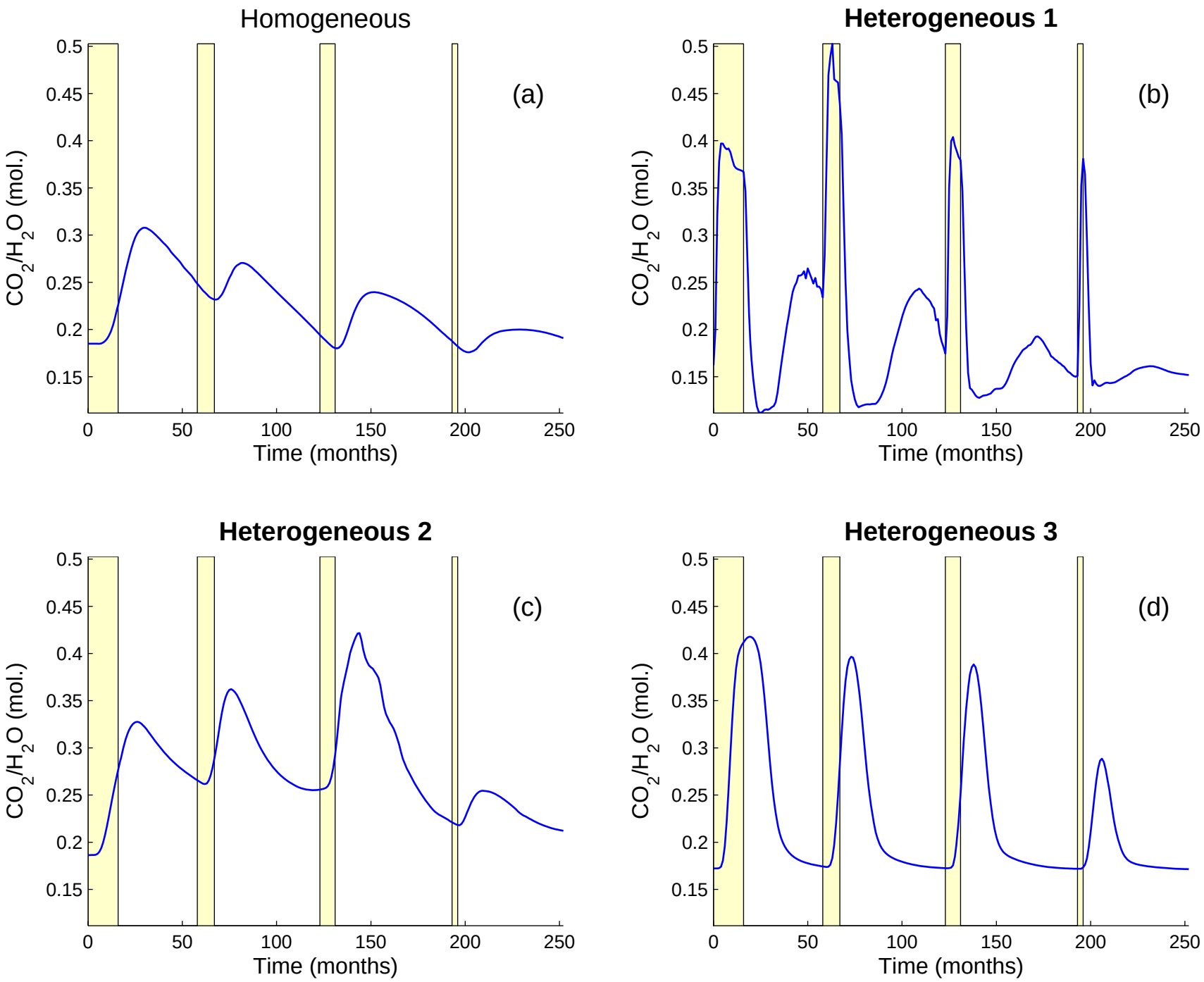
Homogeneous
(a)
Heterogeneous 1
(b)
Heterogeneous 2
(c)
Heterogeneous 3
(d)
CO2/H2O (mol.)
Time (months)
0.5
0.45
0.4
0.35
0.3
0.25
0.2
0.15
0
50
100
150
200
250

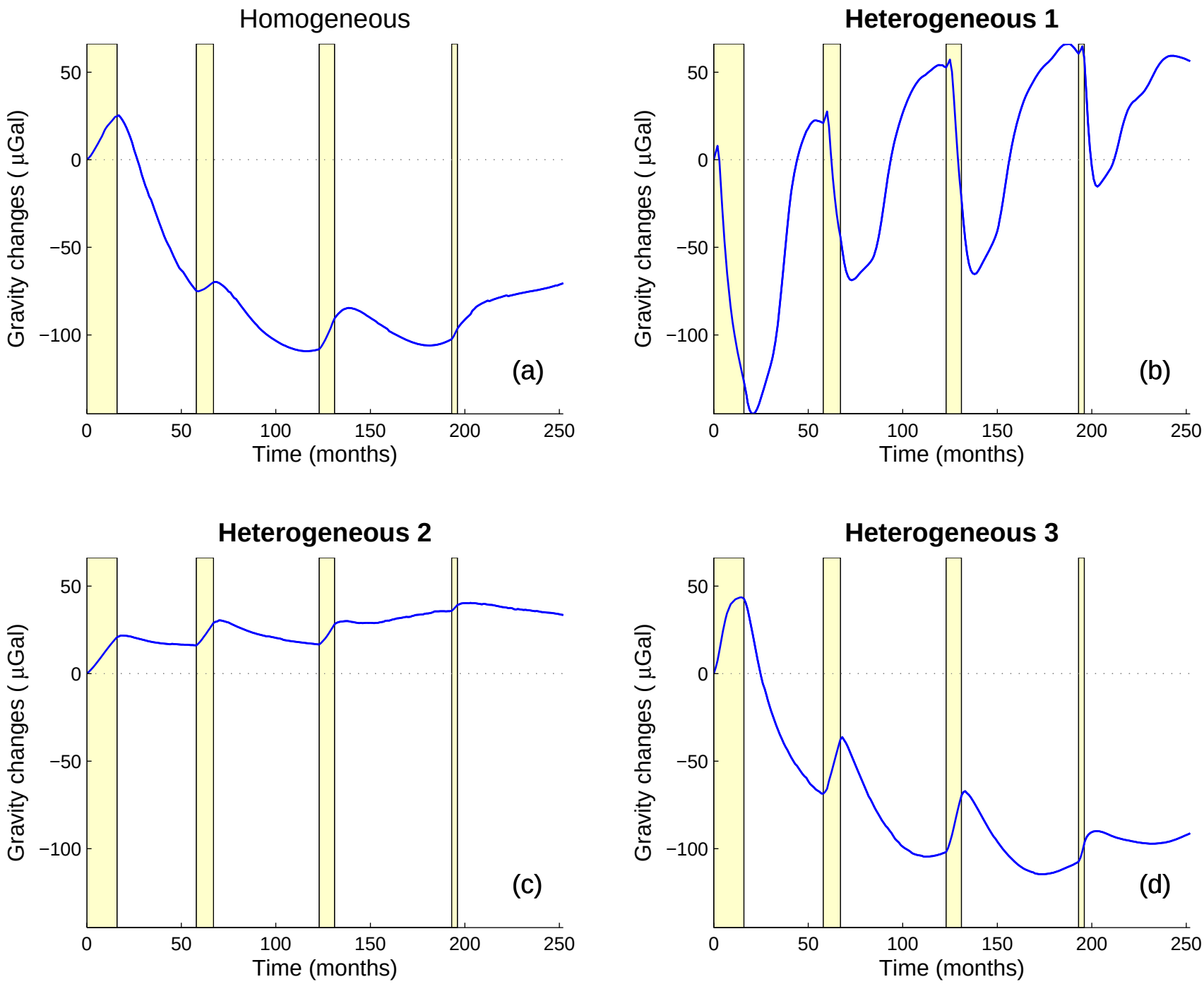
Homogeneous
Heterogeneous 1
Heterogeneous 2
Heterogeneous 3
Gravity changes (µGal)
Time (months)
50
0
−50
−100
0
50
100
150
200
250
(a)
(b)
(c)
(d)

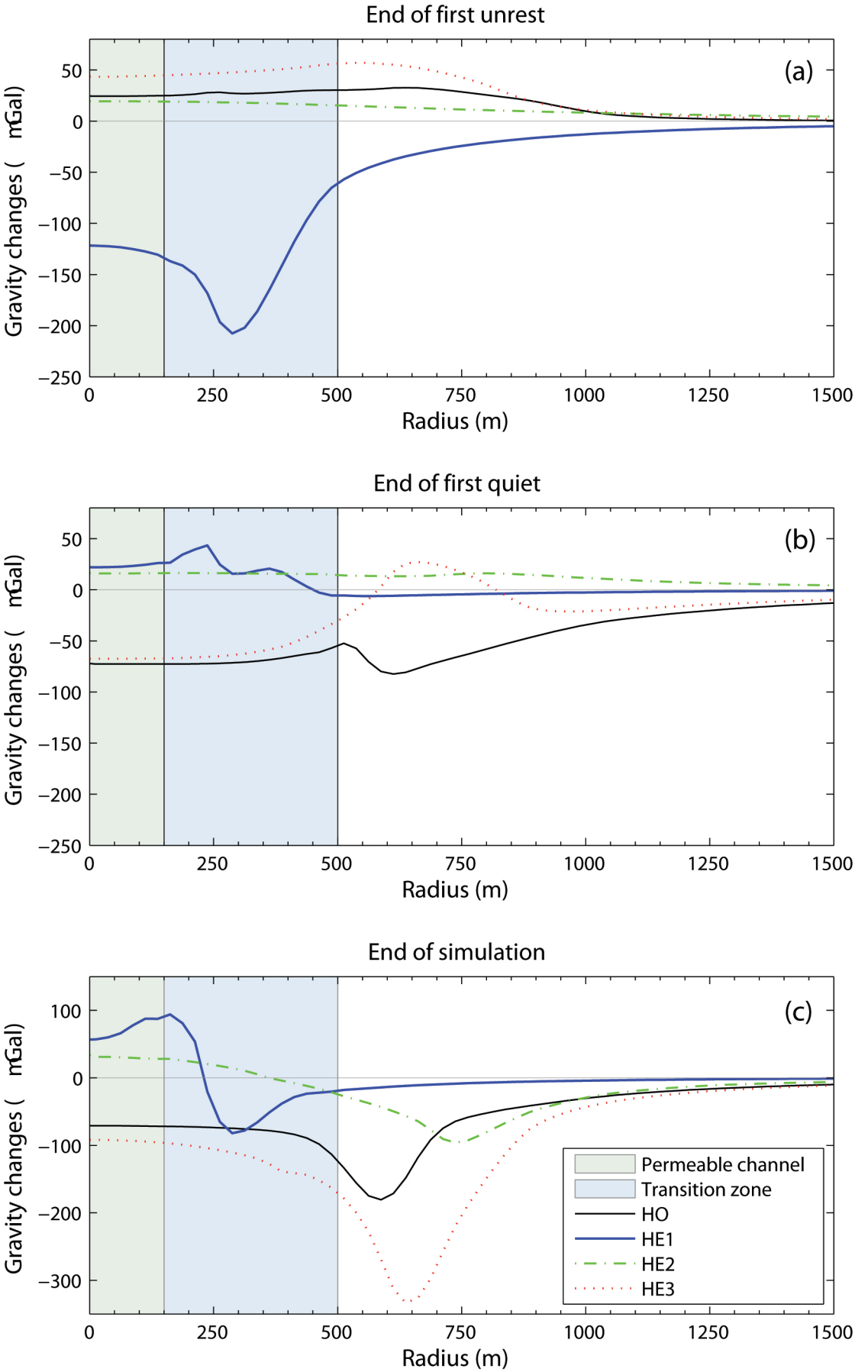
End of first unrest
(a)
Gravity changes (mGal)
50
0
−50
−100
−150
−200
−250
0
250
500
750
1000
1250
1500
Radius (m)
End of first quiet
(b)
Gravity changes (mGal)
Radius (m)
End of simulation
(c)
Gravity changes (mGal)
100
0
−100
−200
−300
Radius (m)
Permeable channel
Transition zone
HO
HE1
HE2
HE3

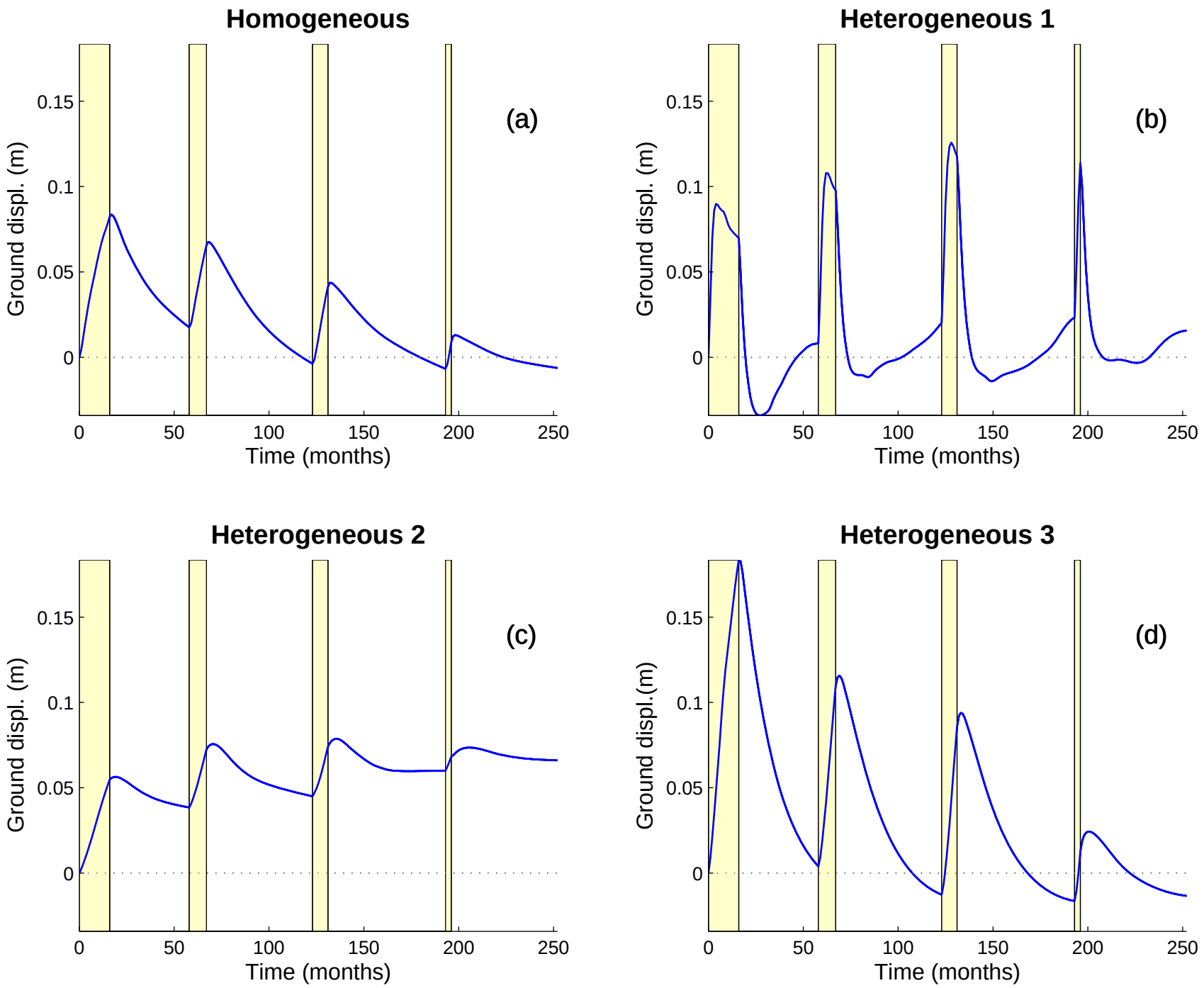
Homogeneous
(a)
Heterogeneous 1
(b)
Heterogeneous 2
(c)
Heterogeneous 3
(d)
Ground displ. (m)
Ground displ.(m)
Time (months)
0
0.05
0.1
0.15
50
100
150
200
250

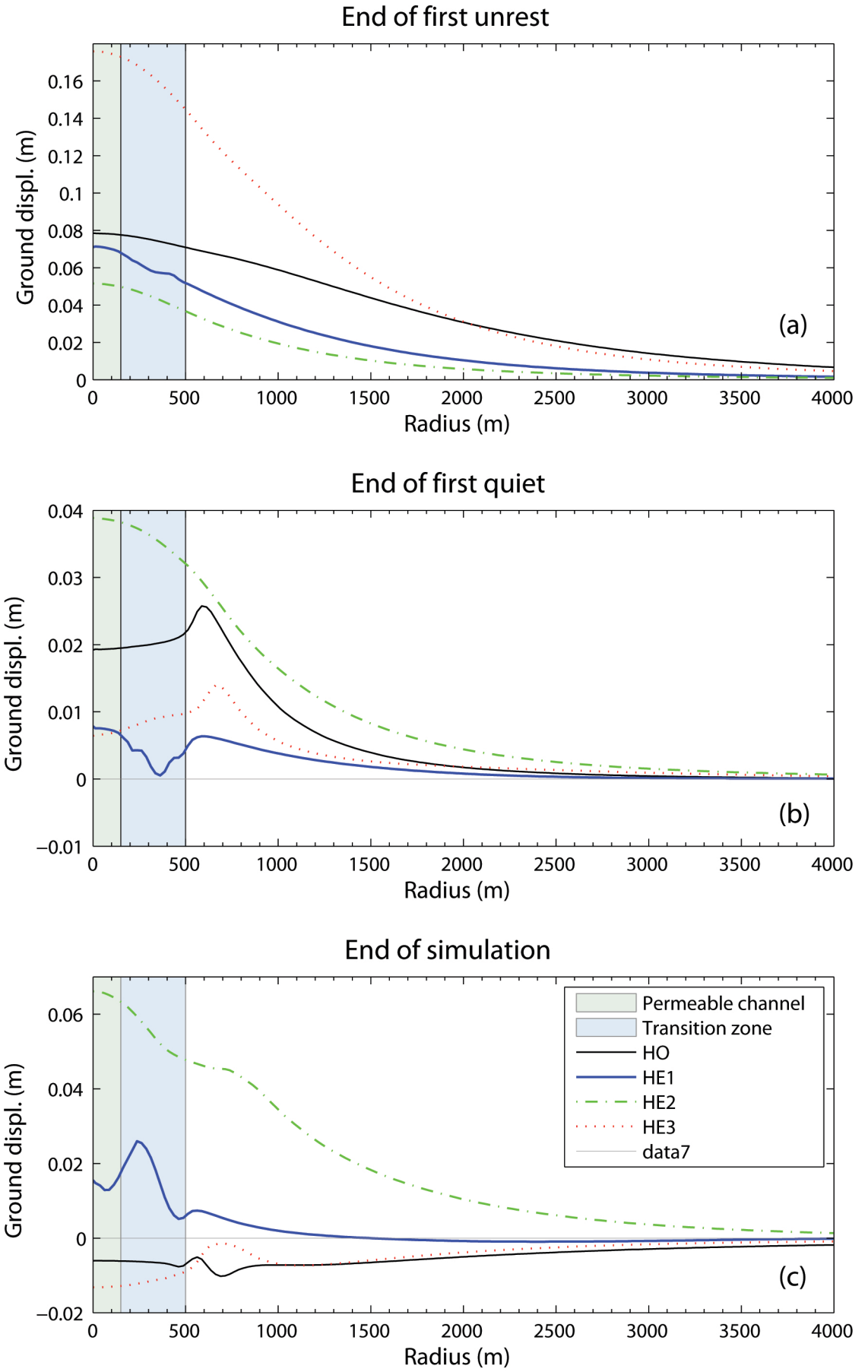
End of first unrest
Ground displ. (m)
Radius (m)
(a)
End of first quiet
Ground displ. (m)
Radius (m)
(b)
End of simulation
Ground displ. (m)
Radius (m)
(c)
Permeable channel
Transition zone
HO
HE1
HE2
HE3
data7